

**Solubility of the hydrated Mg-carbonates nesquehonite and dypingite from 5 to 35°C:  
Implications for CO<sub>2</sub> storage and the relative stability of Mg-carbonates**

Anna L. Harrison<sup>a,b,1\*</sup>, Vasileios Mavromatis<sup>b,c</sup>, Eric H. Oelkers<sup>a,b</sup>, and Pascale Bénézech<sup>b</sup>

<sup>a</sup>Department of Earth Sciences, University College London, Gower Street, WC1E 6BT  
London, United Kingdom (anna.harrison@queensu.ca)

<sup>b</sup>Geoscience and Environment Toulouse (GET), CNRS, UMR 5563, Observatoire Midi-Pyrénées, 14 Avenue Edouard Belin, 31400 Toulouse, France  
(vasileios.mavromatis@get.omp.eu; eric.oelkers@get.omp.eu;  
pascale.benezeth@get.omp.eu)

<sup>c</sup>Institute of Applied Geosciences, Graz University of Technology, Rechbauerstrasse 12,  
8010 Graz, Austria

<sup>1</sup>Present address: Department of Geological Sciences and Geological Engineering and School  
of Environmental Studies, Queen's University, K7L 3N6 Kingston, Canada

\*Corresponding author: anna.harrison@queensu.ca

## 1 **Abstract**

2 Hydrated Mg-carbonate minerals form during the weathering of ultramafic rocks, and  
3 can be used to store atmospheric CO<sub>2</sub> to help combat greenhouse gas-fueled climate change.  
4 Optimization of engineered CO<sub>2</sub> storage and prediction of the composition and stability of  
5 Mg-carbonate phase assemblages in natural and engineered ultramafic environments requires  
6 knowledge of the solubility of hydrated Mg-carbonate phases, and the transformation  
7 pathways between these metastable phases. In this study, we evaluate the solubility of  
8 nesquehonite [MgCO<sub>3</sub>·3H<sub>2</sub>O] and dypingite [Mg<sub>5</sub>(CO<sub>3</sub>)<sub>4</sub>(OH)<sub>2</sub>·(5 or 8)H<sub>2</sub>O] and the  
9 transformation from nesquehonite to dypingite between 5°C and 35°C, using constant-  
10 temperature, batch-reactor experiments. This is the first reported dypingite solubility product.  
11 The logarithm of the solubility product of nesquehonite was determined to be: -5.03±0.13, -  
12 5.27±0.15, and -5.34±0.04 at 5°C, 25°C, and 35°C, respectively. The logarithm of the  
13 solubility product of dypingite was determined to be: -34.95±0.58 and -36.04±0.31 at 25°C  
14 and 35°C, respectively, with eight waters of hydration. The transformation from nesquehonite  
15 to dypingite was temperature-dependent, and was complete within 57 days at 25°C, and 20  
16 days at 35°C, but did not occur during experiments of 59 days at 5°C. This phase  
17 transformation appeared to occur via a dissolution-reprecipitation mechanism; external  
18 nesquehonite crystal morphology was partially maintained during the phase transformation at  
19 25°C, but was eradicated at 35°C. Together, our results facilitate the improved evaluation of  
20 Mg-carbonate mineral precipitation in natural and engineered ultramafic mineral weathering  
21 systems that sequester CO<sub>2</sub>, and for the first time allow assessment of the saturation state of  
22 dypingite in aqueous solutions.

23

- 24 **Keywords:** Mg-carbonates; CO<sub>2</sub> sequestration; mineral solubility; ultramafic mineral
- 25 weathering; mineral phase transformation; dissolution-reprecipitation; dypingite;
- 26 nesquehonite

## 27 **1. Introduction**

28

29         The largest proportion of carbon in Earth's crust is bound in carbonate minerals,  
30 where it is stable over millennia (Sundquist, 1993; Lackner, 2003). The engineered storage of  
31 anthropogenic CO<sub>2</sub> in carbonate minerals is therefore sought to offset greenhouse gas  
32 emissions and mitigate climate change (Lackner et al., 1995; Kelemen and Matter, 2008;  
33 Oelkers and Cole, 2008; Power et al., 2013a, b; Matter et al., 2016). Carbonate mineral  
34 formation during the weathering of silicates and hydroxides is a naturally occurring process,  
35 known as carbon mineralization; this process can be enhanced artificially to store CO<sub>2</sub>.  
36 Several engineered carbon mineralization approaches have been studied at the laboratory  
37 and/or pilot-scale, including injection of CO<sub>2</sub> into subsurface basaltic or ultramafic rock  
38 (Kelemen and Matter, 2008; Power et al., 2013a, b; Gislason and Oelkers, 2014; Matter et al.,  
39 2016), passive or accelerated carbonation of ultramafic mine waste rock and tailings (Wilson  
40 et al., 2006, 2009, 2011, 2014; Power et al., 2010, 2014a; Pronost et al., 2011, 2012; Bea et  
41 al., 2012; Beinlich and Austrheim, 2012; Harrison et al., 2013a, b, 2015, 2016; Oskierski et  
42 al., 2013; Assima et al., 2012, 2014a, b, c; McCutcheon et al., 2015, 2017; Gras et al., 2017),  
43 and accelerated mineralization in high pressure/high temperature *ex situ* reactors (Lackner et  
44 al., 1995; Gerdemann et al., 2007). Enhanced weathering is a related approach that aims  
45 primarily to sequester CO<sub>2</sub> in dissolved form, but can also induce carbonate precipitation. It  
46 entails spreading fine-grained mafic or ultramafic rock in natural weathering environments to  
47 artificially enhance natural weathering (Schuiling and Boer, 2010; Renforth, 2012; Hartmann  
48 et al., 2013; Montserrat et al., 2017; Rigopoulos et al., 2018). Estimation of the CO<sub>2</sub> storage  
49 security of these approaches requires knowledge of the stability, solubility, and formation  
50 pathways of the carbonate mineral products that store the CO<sub>2</sub>. The relative stability and  
51 solubility of several Mg-carbonates has been investigated (Langmuir, 1965; Canterford et al.,

1984; Königsberger et al., 1999; Zhang et al., 2006; Hopkinson et al., 2008, 2012; Hänchen et al., 2008; Xiong and Lord, 2008; Bénézech et al., 2011; 2018; Xiong, 2011; Ballirano et al., 2013; Berninger et al., 2014; Kristova et al., 2014; Gautier et al., 2014). In general, the stability of Mg-carbonates increases from more to less hydrated phases, in the order: lansfordite < nesquehonite < dypingite < hydromagnesite < magnesite (Langmuir, 1965; Canterford et al., 1984). Due to the strong hydration of aqueous Mg, the formation of anhydrous magnesite [MgCO<sub>3</sub>], is kinetically inhibited at low temperatures, and is rarely observed to form on laboratory timescales at temperature less than 60°C (Hänchen et al., 2008; Saldi et al., 2009, 2012; Power et al., 2017). For example, Gautier et al. (2014) demonstrate a 2.5-fold greater growth rate constant for hydromagnesite [Mg<sub>5</sub>(CO<sub>3</sub>)<sub>4</sub>(OH)<sub>2</sub>·4H<sub>2</sub>O] compared to magnesite at 90°C. Thus, ultramafic weathering at the Earth's near-surface is dominated by hydrated Mg-carbonate formation (Shirokova et al., 2013; Power et al., 2014b; Lin et al., 2017), and engineered CO<sub>2</sub> storage efforts at near-Earth's surface temperatures will also tend to form hydrated Mg-carbonates. However, observed mineral assemblages in the field and in laboratory experiments reveal that multiple hydrated magnesium carbonate phases often co-exist, with the more-hydrated phases frequently acting as transient precursors to the more stable, less-hydrated phases (Davies and Bubela, 1973; Hopkinson et al., 2008, 2012; Wilson et al., 2009; Ballirano et al., 2013; Power et al., 2014b; Harrison et al., 2015, 2016). The multitude of potential metastable hydrated phases complicates prediction of Mg-carbonate formation and thus the stability of the CO<sub>2</sub>-storing phase (Königsberger et al., 1999; Hopkinson et al., 2008, 2012; Hänchen et al., 2008; Montes-Hernandez et al., 2012; Kristova et al., 2014). To reduce some of the ambiguity in prediction of Mg-carbonate mineral formation under various conditions, in this study we determine the solubility of nesquehonite [MgCO<sub>3</sub>·3H<sub>2</sub>O] and dypingite [Mg<sub>5</sub>(CO<sub>3</sub>)<sub>4</sub>(OH)<sub>2</sub>·(5 or)8H<sub>2</sub>O], two commonly observed products of carbon mineralization in ultramafic materials

77 (Wilson et al., 2006, 2009, 2011, 2014; Boschi et al., 2009; Zhao et al., 2010; Pronost et al.,  
78 2011; Schaef et al., 2011; Bea et al., 2012; Loring et al., 2012; Montes-Hernandez et al.,  
79 2012; Assima et al., 2012, 2014c; Hövelmann et al., 2012; Felmy et al., 2012; Beinlich and  
80 Austrheim, 2012; Schaef et al., 2013; Harrison et al., 2013a, 2015, 2016, 2017; Power et al.,  
81 2013a, b, c, 2014b; Kristova et al., 2014; McCutcheon et al., 2016; Chaka et al., 2016; Garcia  
82 del Real et al., 2016; Highfield et al., 2016; Gras et al., 2017; McCutcheon et al., 2017), and  
83 the transformation process that converts nesquehonite to dypingite. Both nesquehonite and  
84 dypingite are readily formed during reaction of Mg-rich minerals with CO<sub>2</sub> at ambient  
85 temperatures, with nesquehonite tending to form at greater than atmospheric *p*CO<sub>2</sub> or  
86 evaporative conditions (Königsberger et al., 1999; Power et al., 2007; Xiong and Lord, 2008;  
87 Zhao et al., 2010; Schaef et al., 2011; Harrison et al., 2013a), and dypingite favored under  
88 atmospheric *p*CO<sub>2</sub> (~400 ppm) and microbially-mediated conditions (Power et al., 2007;  
89 Wilson et al., 2010; Mavromatis et al., 2012; Shirokova et al., 2013; Harrison et al., 2013a;  
90 McCutcheon et al., 2016). In addition to their natural occurrence and use for CO<sub>2</sub> storage,  
91 hydrated Mg-carbonates have prompted interest due to their potential formation in engineered  
92 Mg(OH)<sub>2</sub>/MgO barriers for nuclear waste storage (Xiong and Lord, 2008; Xiong, 2011), and  
93 the precipitation of nesquehonite from MgCl<sub>2</sub> brines has been investigated as a way to exploit  
94 Mg resources from salt lakes (Dong et al., 2008; Wang et al., 2008; Cheng et al., 2009;  
95 Cheng and Li, 2009), and as a precursor for high purity MgO production (Cheng et al., 2009;  
96 Wang and Li, 2012). This broad interest in nesquehonite has inspired a number of studies  
97 regarding its thermal stability (Lanas and Alvarez, 2004; Hales et al., 2008; Vágvölgyi et al.,  
98 2008; Ballirano et al., 2010; Jauffret et al., 2015; Morgan et al., 2015), nucleation kinetics  
99 (Cheng and Li, 2010; Zhao et al., 2013), its tendency for solid-solution with transition metals  
100 (Hamilton et al., 2016), and the impacts of temperature, saturation state, and fluid  
101 composition on nucleation and crystal morphology and size (Zhang et al., 2006; Wang et al.,

102 2008; Cheng et al., 2009; Ding et al., 2016). Robie and Hemingway (1972; 1973) determined  
103 its standard heat capacity, standard entropy, and standard enthalpy of formation. Although  
104 several solubility studies of nesquehonite have been conducted both experimentally and  
105 theoretically, they report differing results, or in some cases do not report a solubility product,  
106 instead reporting total aqueous Mg or C concentrations (*c.f.*, Kline, 1929; Kazakov et al.,  
107 1959; Hostetler, 1964; Langmuir, 1965; Königsberger et al., 1999; Dong et al., 2008, 2009;  
108 Wang and Li, 2012). On the other hand, dypingite solubility remains undetermined, despite  
109 its common occurrence in natural and engineered ultramafic weathering environments  
110 (Power et al., 2013a and references therein). Dypingite can be a precursor for the formation  
111 of hydromagnesite (Davies and Bubela, 1973; Hopkinson et al., 2008, 2012; Sutradhar et al.,  
112 2011), a mineral that securely stores CO<sub>2</sub> over tens of thousands of years at Earth's surface  
113 conditions (e.g., Power et al., 2009; 2014). The process by which the metastable Mg-  
114 carbonates transform from less to more stable phases is also an important control on the  
115 isotopic signature of the carbonate minerals, which can be used to trace CO<sub>2</sub> cycling and  
116 sequestration processes (Power et al., 2007, 2014b; Wilson et al., 2009, 2010, 2011, 2014;  
117 Beinlich and Austrheim, 2012; Shirokova et al., 2013; Harrison et al., 2013a, 2016; Oskierski  
118 et al., 2013; Mervine et al., 2014; Falk et al., 2016; Oskierski et al., 2016; Gras et al., 2017).  
119 Similarly, the mobility of toxic metals that can be incorporated in nesquehonite (Hamilton et  
120 al., 2016) will be controlled in part by the efficiency and mechanism of Mg-carbonate phase  
121 transformations.

122         The goals of the present study were to 1) determine the solubility of nesquehonite and  
123 dypingite at conditions relevant to natural and engineered CO<sub>2</sub>-driven weathering, and 2)  
124 assess the nesquehonite-dypingite transformation pathway and the implications for CO<sub>2</sub>  
125 storage.

126

127

## 128 **2. Methods**

129

### 130 *2.1. Nesquehonite and dypingite synthesis*

131 Nesquehonite was synthesized according to a modified method of Robie and  
132 Hemingway (1972), whereby 200 mL of an aqueous 1.8 mol/L  $K_2CO_3$  solution (reagent  
133 grade  $K_2CO_3$ ) was slowly added to a 1000 mL glass beaker containing 200 mL of 1.8 mol/L  
134 aqueous  $MgCl_2$  (NormaPur  $MgCl_2 \cdot 6H_2O$ ). The beaker was then covered with a watch glass  
135 to permit some exchange with laboratory air but limit evaporation and dust inputs. A white  
136 gel-like precipitate was formed immediately upon mixing of the two solutions. This  
137 precipitate was allowed to age in the solution for five days at ambient temperature ( $\sim 22^\circ C$ )  
138 after which the slurry was vacuum-filtered and rinsed multiple times with distilled, de-  
139 ionized water. The precipitate was then dried at ambient temperature for  $\sim 3$  days. Once dry,  
140 the precipitate was gently disaggregated using an agate mortar and pestle, and stored in a  
141 desiccator prior to analysis and use in experiments. The nesquehonite was made in two  
142 separate batches due to the large quantity required, and each was used in separate  
143 experimental runs; a short-term experiment (nesquehonite batch 1), and a long-term  
144 experiment (nesquehonite batch 2). The long-term experiment was conducted subsequent to  
145 the short-term experiment to capture the complete conversion of nesquehonite to dypingite.  
146 Dypingite was synthesized via transformation of the synthetic nesquehonite within the  
147 experiments. The experimental conditions are described in more detail in Section 2.2.

148 The synthetic nesquehonite was characterized using X-ray diffraction (XRD) and  
149 Fourier transform infrared spectroscopy (FTIR), which confirmed the presence of only  
150 nesquehonite in the initial solids used in the experiments (Figures 1 and 2). The empirical  
151 formula of nesquehonite has been debated, and is sometimes reported as



152 [Mg(OH)(HCO<sub>3</sub>)·2H<sub>2</sub>O] (Frost and Palmer, 2011). However, the FTIR spectra collected from  
153 the samples in this study were more consistent with the formula [MgCO<sub>3</sub>·3H<sub>2</sub>O], as the  
154 bicarbonate-derived band at 985 cm<sup>-1</sup> (Zhang et al., 2006) was not present (Figure 1).  
155 Scanning electron microscopy (SEM) (Figure 3) revealed a needle-like morphology typical of  
156 nesquehonite (*c.f.*, Power et al., 2009; Zhao et al., 2010; Schaef et al., 2011; Harrison et al.,  
157 2013a, 2017). Neither XRD nor FTIR data revealed significant differences between the two  
158 batches of synthetic nesquehonite (Figures 1 and 2), though SEM revealed a slightly higher  
159 proportion of fine particles in the second synthesized batch, which was used for the longer-  
160 term experiments.

161

## 162 2.2. *Experimental methods*

163 Experiments to determine the solubility product of nesquehonite were conducted at  
164 constant temperatures of 5°C, 25°C, and 35°C. A single experiment was conducted at 5°C,  
165 whereas duplicate experiments were conducted at 25°C and 35°C. The duplicate experiments  
166 ran subsequently to the originals, and for a longer duration, to ensure the complete  
167 conversion of nesquehonite to dypingite. Each experiment consisted of a suite of nine to  
168 eleven sealed, closed-system reactors. The starting aqueous solution and solid were first  
169 added to the individual reactors (Nalgene bottles) in identical amounts. Each bottle contained  
170 0.6 g of nesquehonite and ~73.4 g of an aqueous solution containing 0.10 M NaCl and 0.06  
171 M NaHCO<sub>3</sub>. At various selected times, an individual reactor was sampled in its entirety  
172 (liquid and solid). This approach was taken to ensure the solid and its contemporaneous fluid  
173 were collected, and to avoid generation of headspace due to sampling, as would occur by  
174 sampling fluids from a single reactor. The individual reactors were filled with minimal  
175 headspace to inhibit loss of CO<sub>2(g)</sub> from solution. To avoid precipitation due to temperature  
176 changes, the experimental solutions were prepared by first heating or cooling distilled, de-

177 ionized water ( $18.2 \text{ M}\Omega \text{ cm}^{-1}$ ) to the desired experimental temperature, followed by the  
178 addition of reagent-grade NaCl and  $\text{NaHCO}_3$  to reach the desired concentration. This aqueous  
179 solution was then poured into the individual reactors, which already contained nesquehonite,  
180 and the reactors were rapidly sealed, weighed, and placed at the experimental temperature.  
181 Experiments conducted at  $5^\circ\text{C}$  were placed on an orbital shaker in a thermostatic refrigerator,  
182 whereas experiments conducted at  $25^\circ\text{C}$  and  $35^\circ\text{C}$  were conducted in shaking water baths at  
183 constant temperature.

184 Individual reactors were sampled one at a time to track the chemical composition of  
185 the reactive aqueous solution, as well as changes in the mineral composition of the solids.  
186 Upon sampling, reactors were weighed to assess evaporative losses and the solution  
187 temperature was measured using a thermometer. The solution was then removed via a syringe  
188 and needle, and filtered with a  $0.22 \mu\text{m}$  polyethersulfone (PES) syringe filter. Two aliquots  
189 were immediately acidified to 2%  $\text{HNO}_3$  for subsequent analysis of Mg concentrations, and a  
190 single aliquot was used for immediate pH measurements, and later alkalinity measurements.  
191 Fluid pH was measured using a Metrohm 913 pH-meter and a Metrohm combined electrode  
192 (6.0234.1000) that was calibrated using NIST traceable  $\text{pH}_{25^\circ\text{C}}$  4.01, 7.00, and 9.18 buffer  
193 solutions at each experimental temperature, with an uncertainty of approximately  $\pm 0.03$  pH  
194 units. Dissolved inorganic carbon concentration was calculated using PHREEQC V3  
195 (Parkhurst and Appelo, 2013) and a modified LLNL database, based on the measured fluid  
196 compositions. Geochemical modeling methods are discussed in further detail in Section 2.4.

197 The solids were separated from any remaining solution via vacuum filtration, and  
198 were rinsed with distilled, de-ionized water to prevent NaCl precipitation. They were then  
199 dried at room temperature for  $\sim 48$  h and stored in a desiccator prior to analysis. Note that  
200 hydrated Mg-carbonate minerals must be stored under dry conditions to prevent their  
201 transformation to other Mg-carbonate minerals in humid air (Davies and Bubela, 1973;

202 Power et al., 2016), therefore care was taken to minimize exposure to laboratory air at all  
203 times.

204 Dypingite was formed *in situ* within the reactors at 25°C and 35°C, with longer-term  
205 experiments designed to allow the complete transformation from nesquehonite to dypingite  
206 and to capture a period of stable solution chemistry representative of equilibrium between the  
207 dypingite and the reactive aqueous solution. The phase transformation was tracked via  
208 changes in aqueous solution composition and mineralogical data collected using XRD  
209 complemented with FTIR for some samples.

210

### 211 2.3. Analytical techniques

212 The alkalinity of all fluid samples was determined by HCl titration using an  
213 automated Schott Titroline Alpha Plus titrator. Long term reproducibility, determined from  
214 repeated analysis of a standard, was better than  $\pm 0.36 \times 10^{-2}$  mol/L ( $3\sigma$ ), and the detection  
215 limit was  $5 \times 10^{-5}$  mol/L. Dissolved inorganic carbon (DIC) concentrations were calculated  
216 using the measured fluid composition and PHREEQC V3 (Parkhurst and Appelo, 2013) with  
217 a modified LLNL database, as described in further detail in Section 2.4. The uncertainty  
218 introduced via the calculation of DIC is unknown; a minimum uncertainty equal to that of the  
219 alkalinity measurement is assumed ( $\pm 0.36 \times 10^{-2}$  mol/L). Aqueous Mg concentrations were  
220 measured by atomic absorption spectroscopy (AAS) using a Perkin Elmer AAnalyst 400.  
221 Samples and standards were matrix-matched in 0.01 mol/L HNO<sub>3</sub>. All samples were  
222 measured in triplicate and reported concentrations represent averages of these measurements,  
223 the standard deviation ( $3\sigma$ ) is smaller than the symbols employed in figures, unless otherwise  
224 shown. Reproducibility was better than 2%, and the quantification and detection limits were  
225  $9.6 \times 10^{-8}$  mol/L and  $2.9 \times 10^{-8}$  mol/L, respectively. Quantification and detection limits were  
226 defined as  $10\sigma$  and  $3\sigma$  over background variation.

227 The mineralogical compositions of the solids were determined using powder XRD  
228 with a Bruker D2 Phaser with Cu radiation. The scan speed was 0.5 s/step, and a step size of  
229 0.02°/step was used. To complement XRD data, FTIR analysis was conducted on select  
230 samples using a ThermoScientific Nicolet iN 10 MX infrared imaging microscope.  
231 Morphological characteristics were examined via scanning electron microscopy using a  
232 JEOL JSM 6360LV or a JEOL JSM 6480LV.

233

#### 234 *2.4. Geochemical modeling*

235 The standard state adopted in this study is that of unit activity at any temperature and  
236 pressure for pure minerals. The standard state for aqueous species at any temperature and  
237 pressure is unit activity of a hypothetical 1 molal solution referenced to infinite dilution.  
238 Aqueous speciation and mineral saturation states were calculated using PHREEQC V3  
239 (Parkhurst and Appelo, 2013) and its LLNL database, which was modified to include the  
240 carbonic acid dissociation constants of Patterson et al. (1982; 1984), the hydrolysis constant  
241 for  $Mg^{2+}$  from Palmer and Wesolowski (1997), the formation constants of  $MgHCO_3^+$  and  
242  $MgCO_3^{\circ}$  ion pairs from Stefansson et al. (2014), the magnesite solubility product from  
243 Bénézeth et al. (2011), the hydromagnesite solubility product from Gautier et al. (2014), and  
244 the brucite solubility product from Brown et al. (1996). Activity coefficients are calculated  
245 using the b-dot model (Helgeson, 1969).

246

### 247 **3. Results**

#### 248 *3.1 Phase transformations*

##### 249 *3.1.1 Phase transformation at 25°C*

250 The measured Mg concentration, pH, alkalinity, mineralogical composition, and the  
251 calculated DIC concentration and aqueous  $Mg^{2+}$ ,  $CO_3^{2-}$ , and  $H_2O$  activities with time in all

252 experiments are listed in Table 1. At 5°C, nesquehonite did not transform into a different  
253 phase throughout the 1420 h (59 d) experiment as confirmed by XRD (Electronic Supplement  
254 (ES) -Figure 1). Similarly, SEM micrographs revealed that the solid phase maintained the  
255 needle-like nesquehonite morphology throughout the experiment (Figure 3).

256 At 25°C, minor dypingite was first detected with XRD at 359 h in the long-term  
257 experiment, and dypingite formed between 367 h and 1086 h during the short-term  
258 experiment (ES-Figures 2 and 3). Trace dypingite was also detected in the 22 h sample in the  
259 long-term 25°C experiment. However, the solution composition did not change, dypingite  
260 was not present in the 122 h sample, nor was it present over this timeframe in the short-term  
261 25°C experiment. Together, this suggests that its presence in the 22 h sample from the long-  
262 term experiment is an artifact of improper sample storage, not dypingite formation in the  
263 experiment.

264 The sample collected at 359 h in the long-term experiment exhibits particles with  
265 needle-like external morphology, similar to the initial nesquehonite, but with rounded edges,  
266 and a flakey, porous surface (Figure 3c). This flakey morphology is typical of dypingite (e.g.,  
267 Canterford et al., 1984; Power et al., 2007; Mavromatis et al., 2012), and suggests the  
268 precipitation of dypingite is closely coupled to the dissolution of nesquehonite at the mineral-  
269 fluid interface, as has been observed for several mineral replacement reactions (e.g., Ruiz-  
270 Agudo et al., 2012 and references therein). Within 1367 h, nesquehonite was completely  
271 replaced by dypingite, which remained until the end of the 2043 h (85 d) long-term  
272 experiment (ES-Figure 3). Dypingite is normally reported in the literature to have the  
273 chemical formula  $[\text{Mg}_5(\text{CO}_3)_4(\text{OH})_2 \cdot 5\text{H}_2\text{O}]$ , but has also been reported to have the formula  
274  $[\text{Mg}_5(\text{CO}_3)_4(\text{OH})_2 \cdot 8\text{H}_2\text{O}]$ , and more rarely  $[\text{Mg}_5(\text{CO}_3)_4(\text{OH})_2 \cdot 6\text{H}_2\text{O}]$  (Raade, 1970;  
275 Canterford et al., 1984; Xiong and Lord, 2008; Hopkinson et al., 2012; Kristova et al., 2014).  
276 The XRD pattern of the dypingite in our experiments was consistent with

277  $[\text{Mg}_5(\text{CO}_3)_4(\text{OH})_2 \cdot 8\text{H}_2\text{O}]$  (International center for diffraction data, pattern PDF-00-029-  
278 0857; ES-Figures 3-5), which differs from that of  $[\text{Mg}_5(\text{CO}_3)_4(\text{OH})_2 \cdot 5\text{H}_2\text{O}]$  (International  
279 center for diffraction data, pattern PDF-00-023-1218), by the presence of a low angle peak at  
280  $2.659^\circ 2\theta$  ( $d = 33.200$ ). Other than this peak, the similarity of the XRD patterns for dypingite  
281 with 5 or 8 hydration waters means the presence of  $[\text{Mg}_5(\text{CO}_3)_4(\text{OH})_2 \cdot 5\text{H}_2\text{O}]$  in addition to  
282  $[\text{Mg}_5(\text{CO}_3)_4(\text{OH})_2 \cdot 8\text{H}_2\text{O}]$  cannot be excluded.

283 An additional phase was observed in the long-term experiment from 599 h until the  
284 end of the experiment; this additional phase is characterized by two small, low-angle peaks  
285 (labeled “d-1” in ES-Figure 3). Dypingite-like phases with varying degrees of hydration and  
286 similar structures, which exhibit low-angle XRD peaks, have been observed in several studies  
287 (Davies and Bubela, 1973; Hopkinson et al., 2008; Hopkinson et al., 2012; Ballirano et al.,  
288 2013; Kristova et al., 2014). For example, during the degassing of a Mg-CO<sub>3</sub> solution at  
289 58°C, Hopkinson et al. (2012) observed what they referred to as several “dypingite-type”  
290 phases with similar crystal structures but different cell volumes and varying numbers of  
291 waters of hydration, including  $[\text{Mg}_5(\text{CO}_3)_4(\text{OH})_2 \cdot 8\text{H}_2\text{O}]$ . Additional peaks not reported in  
292 the established dypingite XRD patterns were also observed at  $\sim 3.5^\circ$  and  $\sim 6^\circ$  by Ballirano et  
293 al. (2013) during the phase transformation of nesquehonite at room temperature. These low  
294 angle peaks and their inconsistent appearance are attributed to the large and varied cell-  
295 volume of dypingite-like phases, different stacking-sequences of the layers of MgO<sub>6</sub> and  
296 carbonate groups, or different water contents (Ballirano et al., 2013). As such, the low angle  
297 peaks observed from 599 h until the end of the experiment, are attributed to an additional  
298 dypingite-like phase, potentially differing in cell volume and/or number of hydration waters.  
299 To further evaluate the dypingite-like phase documented at 25°C, the FTIR spectrum of a  
300 sample containing this phase (25°C, 1607 h) was compared to the FTIR spectrum of a sample  
301 from the long-term 35°C experiment, which contained only XRD-identifiable dypingite

302 (35°C, 560 h). The FTIR spectra are close to identical (Figure 1), consistent with the  
303 interpretation that the unnamed phase documented in the 25°C experiments is likely another  
304 dypingite-like phase.

305 Changes in fluid composition were coincident with the phase transformation  
306 documented with XRD. During the phase transformation, pH decreased from ~9.2 to ~8.8  
307 between 120 h and 599 h before stabilizing at ~8.8 for the remainder of the experiment  
308 (Figures 4a and 4d). This suggests that the phase transformation consumes protons despite  
309 forming a hydroxyl-bearing phase. The Mg concentration exhibited a minor decrease during  
310 the phase transformation (Figures 4b and 4e), whereas the DIC exhibited a slight increase  
311 (Figures 4c and 4f). After 599 h, DIC and Mg concentration again remained stable for the  
312 remainder of the experiment (Figures 4b and 4c).

313

### 314 *3.1.2. Phase transformation at 35°C*

315 At 35°C, the transformation from nesquehonite to dypingite was more rapid than at  
316 25°C. Dypingite was first detected at trace levels by XRD in the 75 h sample from the short-  
317 term experiment (ES-Figure 4), and in the 123 h sample from the long-term experiment (ES-  
318 Figure 5). Similar to the 25°C experiment, the dypingite XRD pattern was consistent with  
319 that of  $[\text{Mg}_5(\text{CO}_3)_4(\text{OH})_2 \cdot 8\text{H}_2\text{O}]$  (International center for diffraction data, pattern PDF-00-  
320 029-0857; ES-Figures 4 and 5). The additional dypingite-like phase observed at 25°C was not  
321 evident in the 35°C experiments, however, a different unidentified phase was recorded in the  
322 sample at 718 h in the long-term experiment (identified as “unknown” in ES-Figure 5),  
323 evidenced by additional peaks at ~27° and ~33° and the disappearance of the ~11° peak. It is  
324 not clear whether this was an additional phase, or representative of a change in the dypingite  
325 structure. This phase was not present before or after 718 h, nor was it detected in the short-  
326 term experiment. It may be an artifact of imperfect sample storage, rather than reflecting an

327 *in situ* mineralogical change in the reactors. However, if there were a mineral phase change  
328 within the reactor, that would impact solubility calculations. Thus, this sample was not  
329 included in calculation of the solubility product. Nesquehonite was no longer present within  
330 482 h at 35°C (ES-Figure 5), compared to 1367 h for complete conversion of nesquehonite at  
331 25°C.

332 SEM images revealed a different evolution of crystal morphology between the 25°C  
333 and 35°C experiments; unlike at 25°C, the external crystal morphology of nesquehonite was  
334 not maintained. Rather, over a similar time-frame, the needle-like morphology was replaced  
335 by flakey aggregates with typical dypingite morphology (Figure 3d) (*e.g.*, Canterford et al.,  
336 1984; Power et al., 2007; Mavromatis et al., 2012). This difference in morphological  
337 evolution may be a consequence of the different reaction rates. In both cases, the morphology  
338 change suggests the mineral phase transformation occurs via dissolution-reprecipitation.  
339 However, the slower rate of nesquehonite dissolution at 25°C coupled to the rapid re-  
340 precipitation as dypingite could result in the observed pseudo-morphic replacement at this  
341 temperature. Conversely, a relatively high nesquehonite dissolution rate compared to  
342 dypingite precipitation rate at 35°C, would allow a spatial and thus morphological separation  
343 of the two phases.

344 Similar to the fluid composition change observed during the phase transformation at  
345 25°C, the pH, Mg concentration, and DIC concentration evolved during the nesquehonite-  
346 dypingite transformation at 35°C (Figure 4). A decrease in pH from ~9.15 to ~8.66 occurred  
347 between ~74 h and 482 h (Figures 4a and 4d), while a slight decline in Mg concentration was  
348 observed after 310 h (Figures 4b and 4e). The decline in Mg concentration occurred when the  
349 solids became dominated by dypingite, rather than by nesquehonite (Table 1). A slight  
350 decrease in Mg concentration continued for the remainder of the 35°C experiment, suggesting  
351 either a slow approach to dypingite equilibrium, or perhaps the beginning of a transformation



352 to a less hydrated Mg-carbonate, though no further mineralogical changes were detected with  
353 XRD or FTIR. A minor increase in DIC concentration was observed after 75 h (Figures 4c  
354 and 4f), but DIC was again fairly constant from ~243 h to the end of the short- and long-term  
355 experiments. The short-term experiments were too brief for completion of the nesquehonite-  
356 dypingite transformation, but the trends in fluid composition were consistent with the early  
357 stages of the transformation documented in the longer-term experiments.

358

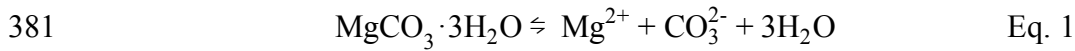
### 359 *3.2 Retrieval of the nesquehonite solubility product*

360 The dissolution of nesquehonite to a constant fluid composition was rapid in all  
361 experiments, with pH, Mg, and alkalinity increasing to constant values within 120 h, 24 h,  
362 and 3 h in the 5°C, 25°C, and 35°C experiments, respectively (Table 1; Figure 4). The values  
363 used for the calculation of nesquehonite and dypingite solubility products at all temperatures  
364 are indicated in Table 1. Brucite [Mg(OH)<sub>2</sub>], which can form at room temperature from Mg-  
365 rich solutions, remained undersaturated in all experiments. Nesquehonite was the only phase  
366 detected with XRD throughout the 5°C experiment (ES-Figure 1), therefore all samples taken  
367 from 120 h, when the fluid composition stabilized, up to the end of the experiment (1420 h)  
368 were included in the calculation of its solubility product ( $K_{sp}^{nsq}$ ). In the 25°C experiment,  
369 nesquehonite was the only phase detectable with XRD for 367 h in the short-term experiment  
370 (ES-Figure 2), though minor dypingite was detected at 359 h in the long-term experiment  
371 (ES-Figure 3). Solution compositions remained relatively constant over these time periods,  
372 therefore samples from between 24 h and 367 h in the short-term experiment, and less than  
373 359 h in the long-term experiment were used for the calculation of  $K_{sp,25}^{nsq}$ , providing a total  
374 of six distinct points for which the solubility product was calculated and averaged.

375 In the 35°C experiment, the solubility product was calculated using the aqueous  
376 solution composition between 3 h and 24 h in the short-term experiment, and 26 h and 74 h in

377 the long-term experiment (seven time points in total), representing time points that had  
378 constant fluid composition and no detectable dypingite (Table 1).

379 The nesquehonite solubility product was determined using the average of the  
380 calculated  $Mg^{2+}$  and  $CO_3^{2-}$  aqueous activities according to the reaction



382 and its law of mass action

383 
$$K_{sp}^{nsq} = a_{Mg^{2+}} a_{CO_3^{2-}} a_{H_2O}^3 \quad \text{Eq. 2}$$

384

385 The aqueous activities in equation 2 were calculated using PHREEQC V3 with the modified  
386 LLNL database, as described in section 2.4, and are listed in Table 1. The nesquehonite  
387 solubility products are reported in Table 2.

388 Based on the solubility product determined in this study, the standard molar Gibbs  
389 free energy of formation of nesquehonite was also calculated. The standard state properties of  
390 the aqueous species involved in equation 1 were used, and are listed in Table 3. The enthalpy  
391 of the nesquehonite dissolution reaction (equation 1) was estimated by plotting the natural  
392 logarithm of the solubility product versus reciprocal temperature (Figure 5, as shown with  
393 base 10 logarithm), with the slope of the line equated to  $-\Delta H_r^\circ/R$ , where  $\Delta H_r^\circ$  is the enthalpy  
394 of reaction, and  $R$  is the ideal gas constant (Table 3). The standard enthalpy of formation of  
395 nesquehonite was then calculated using the standard state properties of the aqueous species  
396 involved in equation 1, as listed in Table 3.

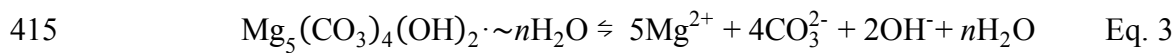
397

### 398 *3.3 Retrieval of the dypingite solubility product*

399 The solubility product of dypingite ( $K_{sp}^{dyp}$ ) was estimated from the long-term 25°C  
400 and 35°C experiments in which complete transformation to dypingite was achieved.

401 Dypingite was not formed at 5°C, likely due to slower kinetics of the transformation reaction,

402 thus its solubility product was not determined at this temperature. At 25°C, nesquehonite was  
 403 no longer detected after 1367 h (Table 1; ES-Figure 3), and the fluid composition was  
 404 relatively constant for the remainder of the experiment. This period is therefore taken to  
 405 reflect equilibrium between dypingite and the aqueous solution, and the solubility product  
 406 was calculated from the final three samples from this experiment (Table 1). At 35°C,  
 407 nesquehonite was no longer detected after 482 h (Table 1; ES-Figure 5); the fluid  
 408 composition also remained relatively constant for the remainder of the experiment. The fluid  
 409 composition from 482 h until the end of the experiment was therefore used to calculate  $K_{sp}^{dyp}$   
 410 (Table 1), except for the sample taken at 718 h, due to the presence of an unidentified phase  
 411 in the solid sample as previously described. A total of five distinct points were used for the  
 412 solubility product calculation at 35°C. Aqueous activities of  $Mg^{2+}$  and  $CO_3^{2-}$  were calculated  
 413 using PHREEQC V3 and the modified LLNL database, and  $OH^-$  activity was calculated from  
 414 pH measurements. The  $K_{sp}^{dyp}$  was calculated using these values and equations 3 and 4.



416

417 
$$K_{sp}^{dyp} = a_{Mg^{2+}}^5 a_{CO_3^{2-}}^4 a_{OH^-}^2 a_{H_2O}^n \quad \text{Eq. 4}$$

418 where the variable,  $n$ , was 5 or 8. The presence of at least two dypingite-like phases in the  
 419 25°C experiments, and potentially both  $[Mg_5(CO_3)_4(OH)_2 \cdot 5H_2O]$  and  
 420  $[Mg_5(CO_3)_4(OH)_2 \cdot 8H_2O]$  in the 35°C experiments means that the value calculated for the  
 421 dypingite solubility product likely represents a mixture of dypingite-like phases of varying  
 422 degrees of hydration. Due to the uncertainty in the exact hydration state of dypingite, and the  
 423 presence of an additional dypingite-like phase at 25°C, the  $K_{sp}^{dyp}$  was calculated in three  
 424 ways. Either the activity of water was assumed to be unity, or the activity of water was  
 425 calculated based on the solution composition using PHREEQC V3, and  $K_{sp}^{dyp}$  was

426 determined using eight or five waters of hydration and equation 4. These are the most  
427 commonly reported stoichiometries for dypingite and have XRD patterns that are consistent  
428 with our experimental data. The  $K_{sp}^{dyp}$  values calculated in each case were equivalent within  
429 error (Table 2), demonstrating that uncertainty in the hydration state of dypingite does not  
430 strongly affect the  $K_{sp}^{dyp}$  retrieved at the experimental ionic strength. The solubility product  
431 (Table 2) decreased slightly with increasing temperature, consistent with the behavior of  
432 nesquehonite (this study) and hydromagnesite  $[\text{Mg}_5(\text{CO}_3)_4(\text{OH})_2 \cdot 4\text{H}_2\text{O}]$  (Gautier et al.,  
433 2014).

434

#### 435 **4. Discussion**

##### 436 *4.1 Nesquehonite and dypingite solubility products*

437 The standard molar Gibbs free energy of formation of nesquehonite calculated from  
438 our data was in very good agreement with that determined by Robie and Hemingway (1973),  
439 and Langmuir (1965), and the standard molar enthalpy of formation calculated from our data  
440 was in very good agreement with Robie and Hemingway (1973) (Table 3). The nesquehonite  
441 solubility product calculated from our data decreases slightly with increasing temperature,  
442 consistent with the solubility of other Mg- and Ca-carbonate minerals (Table 2) (e.g.,  
443 Königsberger et al., 1999; Marion, 2001; Bénézech et al., 2011, 2018; Gautier et al., 2014),  
444 and temperature dependence reported for nesquehonite solubility in previous studies (Dong et  
445 al., 2008; Wang and Li 2012). However, the temperature dependence is not significant outside  
446  $3\sigma$  uncertainty (Table 2; Figure 5). Our values are in good agreement with those reported in  
447 the modeling study of Wang and Li (2012), which considered the impact of aqueous  
448 speciation on nesquehonite solubility in saline solutions (Table 2). However, discrepancies  
449 are evident between our values and some of the corresponding values at 25°C reported in the  
450 literature; values in the present study fall between those of Kline (1929), Langmuir (1965),

451 and Hostetler (1964) (Table 2; Figure 5); such differences could be attributed to differences  
452 in the calculation of aqueous speciation. The  $\log K_{sp}^{nsq}$  in both the LLNL and minteqv4  
453 PHREEQC databases are most similar to that of Kline (1929), and are considerably larger  
454 than those measured in this study as well as the values reported by Langmuir (1965) and  
455 Hostetler (1964) (Table 2; Figure 5). In addition, the temperature extrapolation employed in  
456 both of these databases exhibits a stronger temperature dependence than that measured in the  
457 present study, or that indicated by Wang and Li (2012) (Figure 5). The neglect of aqueous  
458 speciation in the calculation of the solubility product of Kline (1929) likely explains the  
459 discrepancy between this value and that calculated in our study, as also suggested by  
460 Langmuir (1965) to explain differences between reported nesquehonite solubility products.  
461 The reason for the discrepancy between our measured values and those reported by Hostetler  
462 (1964) and Langmuir (1965) is less clear, but may again relate to differences in the treatment  
463 of aqueous speciation. Robie and Hemingway (1973) suggest that the calorimetric data from  
464 their study are only in agreement with the solubility data of Langmuir (1965) if the aqueous  
465 complexation assumed by Langmuir (1965) is overestimated. This could also account for the  
466 discrepancy between the Langmuir (1965) value and that calculated here. As, the present  
467 study used recent data for the complexation of aqueous Mg-carbonate species (Stefansson et  
468 al., 2014), which were not available at the time of the Hostetler (1964) and Langmuir (1965)  
469 studies and much of the data regarding aqueous Mg-carbonate complex stability came after  
470 these studies (Stefansson et al., 2014 and references therein). In addition, the reported  
471 stability of  $\text{MgCO}_3^\circ$  and  $\text{MgHCO}_3^+$  aqueous complexes at 25°C reported in early literature  
472 was highly variable (Stefansson et al., 2014). It is therefore unsurprising that solubility  
473 products determined for magnesium carbonates like nesquehonite differ between studies that  
474 used different thermodynamic data for aqueous speciation. The similarity between the Kline  
475 (1929) value and those used in the LLNL and minteqv4 databases suggests they may also

476 lack consideration of aqueous complexation, thus we propose that values reported in the  
477 present study and by Wang and Li (2012) are more appropriate for calculating nesquehonite  
478 saturation state.

479 The dypingite solubility product has not previously been reported, therefore our  
480 calculated  $K_{sp}^{dyp}$  cannot be compared with other dypingite values. Instead, we compare our  
481  $K_{sp}^{dyp}$  values to those of hydromagnesite, a structurally similar but less hydrated Mg-  
482 carbonate. Our calculated  $K_{sp}^{dyp}$  is higher than those reported for hydromagnesite at 25°C:  
483  $K_{sp,25}^{hmg} = 10^{-37.08}$  (Gautier et al., 2014), and  $10^{-41.56}$  (Xiong, 2011), compared to  $K_{sp,25}^{dyp,8H2O} =$   
484  $10^{-34.95 \pm 0.58}$ . This is consistent with previous observations of dypingite behavior, as it is  
485 commonly observed to transform to hydromagnesite over time (Davies and Bubela, 1973;  
486 Hopkinson et al., 2008, 2012; Sutradhar et al., 2011; Ballirano et al., 2013), reflecting its  
487 instability compared to hydromagnesite and therefore its higher solubility product. Using our  
488 dypingite and nesquehonite solubility products, it can be shown that hydromagnesite is more  
489 stable than both of these phases across a broad range of pH and  $pCO_2$  conditions (Figure 6).  
490 However, the relative stability of dypingite and nesquehonite is sensitive to pH for a fixed  
491 DIC concentration (Figure 6). At higher pH there is a greater difference in their relative  
492 stability, with dypingite being more stable than nesquehonite, whereas a smaller difference is  
493 predicted at low pH, owing to the sensitivity of the dypingite solubility product to the activity  
494 of  $OH^-$  (Figure 6).

495

#### 496 *4.2 Implications*

497 Dypingite and nesquehonite are common weathering products of ultramafic rock  
498 (Wilson et al., 2006, 2009, 2014; Power et al., 2007; Beinlich and Austrheim, 2012; Garcia  
499 del Real et al., 2016; Lin et al., 2017), and are documented  $CO_2$  sinks that can be used to  
500 store  $CO_2$  (Power et al., 2007, 2013a, b, c, 2016; Pronost et al., 2011; Bea et al., 2012;

501 Assima et al., 2012, 2014c ; Harrison et al., 2013a, 2015, 2016, 2017; Wilson et al., 2014;  
502 McCutcheon et al., 2014; Morgan et al., 2015; Hamilton et al., 2016, 2018; Gras et al.,  
503 2017). Yet, a lack of dypingite solubility data has hindered the ability to evaluate and predict  
504 its formation (Power et al., 2007, 2013c, 2014b; Wilson et al., 2010; Mavromatis et al., 2012;  
505 Harrison et al., 2013a; McCutcheon et al., 2014). The results presented in this study allow  
506 better estimation of dypingite stability in aqueous solution. For example, the solubility  
507 products determined in this study were added to PHREEQC V3 and used to calculate the  
508 dypingite saturation state in a previous experimental study in which it formed (Mavromatis et  
509 al., 2012), and in a natural wetland in Atlin, Canada, where it has been observed to form in  
510 microbial mats (Power et al., 2007, 2009, 2014b). In the experimental study (Mavromatis et  
511 al., 2012), dypingite was somewhat supersaturated, suggesting that despite forming more  
512 readily at low temperature than hydromagnesite, its precipitation is nevertheless somewhat  
513 kinetically inhibited (Table 4). In the natural wetlands, where dypingite has both been  
514 directly observed as well as precipitated in experiments using water from the wetlands  
515 (Power et al., 2007, 2014b), dypingite was very close to equilibrium (Table 4), providing  
516 confidence in our  $K_{sp}^{dyp}$ . The  $K_{sp}^{dyp}$  determined in the present study can therefore be used to  
517 better constrain the possibility of dypingite precipitation in natural environments, and during  
518 engineered CO<sub>2</sub> storage operations. Note also that the nesquehonite solubility products in the  
519 PHREEQC databases appear to underestimate the stability of this mineral compared to the  
520 results of recent studies (this study; Wang and Li, 2012), and may thus underestimate its  
521 likelihood to form.

522         The main goal of engineered CO<sub>2</sub> storage operations is to ensure CO<sub>2</sub> is stored in a  
523 stable form and will not be substantially released over thousand-year timescales. Therefore,  
524 the design of CO<sub>2</sub> storage strategies to produce stable carbonate minerals is a key  
525 consideration, and has motivated numerous studies on the relative stability of Mg-carbonate

526 minerals (Königsberger et al., 1999; Lanas and Alvarez, 2004; Hales et al., 2008; Hopkinson  
527 et al., 2008, 2012; Vágvölgyi et al., 2008; Hänchen et al., 2008; Frost et al., 2008; Ballirano  
528 et al., 2010; Ballirano et al., 2013; Kristova et al., 2014; Jauffret et al., 2015; Morgan et al.,  
529 2015). The stoichiometry of minerals in terms of their Mg:C ratios and Mg:H<sub>2</sub>O ratios also  
530 governs the efficiency of CO<sub>2</sub> sequestration; a Mg:C ratio of 1:1 such as provided by  
531 nesquehonite, lansfordite [MgCO<sub>3</sub>·5H<sub>2</sub>O], and magnesite is most efficient. In dry conditions,  
532 such as in subaerially stored ultramafic mining wastes (Bea et al., 2012; Wilson et al., 2014),  
533 or near the injection of supercritical CO<sub>2</sub> in the subsurface (Schaefer et al., 2011, 2013; Chaka  
534 et al., 2016), the availability of water may be a limiting factor for carbonate precipitation  
535 (Schaefer et al., 2011, 2013; Harrison et al., 2015, 2016), therefore carbonates that consume  
536 less water during their formation, such as dypingite, hydromagnesite, and magnesite, are  
537 desirable. The anhydrous carbonate, magnesite, is the ideal carbon sink in terms of stability,  
538 water requirements, and efficiency (Power et al., 2017). However, as it does not tend to form  
539 at low temperatures (Hänchen et al., 2008; Saldi et al., 2012), the hydrated carbonates are the  
540 targets for near Earth's surface temperature carbon storage. Although nesquehonite tends to  
541 precipitate from CO<sub>2</sub>-rich solutions and under evaporative conditions (Königsberger et al.,  
542 1999; Power et al., 2007; Zhao et al., 2010; Harrison et al., 2013a), it readily transforms on  
543 hour- to month-long time scales to either dypingite or hydromagnesite, depending on the  
544 temperature. This transformation is accompanied by a slight loss of CO<sub>2</sub> to solution, as  
545 documented in the experiments at 25°C and 35°C (Figure 4c and 4f), which is less ideal for  
546 CO<sub>2</sub> storage. On the other hand, the transformation from dypingite to the more stable phase,  
547 hydromagnesite, does not result in a loss of CO<sub>2</sub> (Ballirano et al., 2013), therefore this  
548 mineral phase transformation minimizes loss of stored CO<sub>2</sub>. This suggests dypingite is a good  
549 target mineral for CO<sub>2</sub> storage at low temperatures. The tendency for dypingite to form over  
550 nesquehonite at atmospheric *p*CO<sub>2</sub> (~400 ppm), suggests that air capture coupled with



551 carbonate mineral precipitation inherently produces a CO<sub>2</sub> sink of higher stability, though the  
552 relatively low concentration of CO<sub>2</sub> in ambient air compared to CO<sub>2</sub> point sources means that  
553 carbon mineralization rates can be limited by the availability of CO<sub>2</sub> (Wilson et al., 2010; Bea  
554 et al., 2012; Pronost et al., 2012; Harrison et al., 2013b; Wilson et al., 2014). Microbially-  
555 mediated carbonate precipitation also tends to favor dypingite precipitation (Power et al.,  
556 2007; Mavromatis et al., 2012; McCutcheon et al., 2016), highlighting that microbially-  
557 mediated carbonation is a highly promising strategy for carbon mineralization at near Earth's  
558 surface conditions.

559 Ultramafic rock such as serpentinite contributes disproportionately to the release of  
560 chromium globally during natural weathering processes compared to other rock-types, owing  
561 to its high reactivity and high chromium content (McClain and Maher, 2016; Beinlich et al.,  
562 2018). It has recently been observed that secondary Mg-carbonate minerals formed during the  
563 weathering of ultramafic rock can help to mitigate the release of metals such as chromium,  
564 due both to incorporation of the metals into the carbonate minerals, and trapping of  
565 particulates within carbonate cement (Hamilton et al., 2016; Hamilton et al., 2018). The  
566 relative stability and mechanism of phase transformations is highly relevant to the cycling of  
567 potential contaminants like chromium in both natural and engineered ultramafic weathering  
568 environments. The change in mineral structure between nesquehonite and dypingite, and the  
569 alteration of crystal morphology during the phase transformation is indicative of a  
570 dissolution-reprecipitation process. This implies that metals initially stored in nesquehonite  
571 may be released to solution, and may or may not be equally reincorporated into dypingite,  
572 depending on the relative affinity for metals between the two phases. Similarly, isotopic  
573 signatures, which can be used as tracers for CO<sub>2</sub> cycling in natural ultramafic environments  
574 and mine wastes (Power et al., 2007; Wilson et al., 2009, 2010, 2011, 2014; Beinlich and  
575 Austrheim, 2012; Shirokova et al., 2013; Harrison et al., 2013a, 2016; Oskierski et al., 2013,

576 2016; Mervine et al., 2014; Mavromatis et al., 2015; Falk et al., 2016; Gras et al., 2017;  
577 Oelkers et al., 2018), may be reset during mineral phase transformations that occur via  
578 dissolution-reprecipitation, complicating their interpretation.

579

## 580 **5. Conclusions**

581 The hydrated Mg-carbonate minerals nesquehonite and dypingite are common  
582 products of natural and engineered ultramafic rock weathering, and are of interest owing to  
583 their capacity to securely store atmospheric CO<sub>2</sub>. Knowledge of their stability, longevity, and  
584 consequences of transformations will aid in our ability to ascertain the longevity and capacity  
585 of engineered carbon storage operations. In this study, the solubility of nesquehonite was re-  
586 examined, and the solubility of dypingite was measured for the first time. Our nesquehonite  
587 solubility product is in good agreement with the recent modeling study of Wang and Li  
588 (2012), which considered aqueous speciation. Our dypingite solubility product, though  
589 complicated by the presence of multiple dypingite-like phases, nevertheless allows estimation  
590 of dypingite saturation state in natural waters and engineered CO<sub>2</sub> storage operations. A  
591 natural wetland where dypingite has been observed (Power et al., 2007, 2009, 2014) is  
592 demonstrated to be close to equilibrium with respect to dypingite, providing confidence in  
593 our values. Finally, our experimental results indicate that nesquehonite, which tends to form  
594 at greater than atmospheric  $p\text{CO}_2$ , can rapidly transform to dypingite at 25°C and 35°C,  
595 resulting in greater security of CO<sub>2</sub> storage due the higher stability of this phase, but  
596 accompanied by a slight loss of CO<sub>2</sub> to solution. This phase transformation apparently occurs  
597 via a dissolution re-precipitation mechanism, altering external crystal morphology,  
598 potentially releasing trace metals, and likely resetting isotopic signatures.

599

## 600 **Acknowledgments**

601

602           This research was funded by a Marie Skłodowska-Curie Individual Fellowship  
603 awarded to ALH under grant agreement number 701478 (DryMIN) under the European  
604 Union's Horizon 2020 program, and partly by a postdoctoral fellowship from the Natural  
605 Sciences and Engineering Research Council of Canada. This study also benefited from the  
606 financial support of the ISIFoR Carnot institute (Institute for the Sustainable Engineering of  
607 Fossil Resources) under the project SERPCARB AAP-2016. The manuscript was improved  
608 by suggestions from two anonymous reviewers. Michel Thibaut and Ludovic Menjot are  
609 thanked for their assistance with XRD. We appreciate the assistance of Thierry Aigouy,  
610 Stephane Le Blond du Plouy, and James Davy with SEM, and of Carole Causserand with  
611 analyses of fluids. Andrew Thomson is thanked for access to and assistance with FTIR,  
612 which was supported by the Science and Technology Facilities Council under grant number  
613 ST/K000934/1. Alain Castillo is thanked for his assistance with laboratory apparatus and  
614 Sasha Wilson for valuable advice regarding XRD data. Ian Power generously provided fluid  
615 compositions for the wetland in Atlin, Canada.

616 **References**

617

618 Assima G. P., Larachi F., Beaudoin G. and Molson J. (2012) CO<sub>2</sub> sequestration in chrysotile  
619 mining residues—Implication of watering and passivation under environmental  
620 conditions. *Ind. Eng. Chem. Res.* **51**, 8726–8734.

621 Assima G. P., Larachi F., Molson J. and Beaudoin G. (2014a) Comparative study of five  
622 Québec ultramafic mining residues for use in direct ambient carbon dioxide mineral  
623 sequestration. *Chem. Eng. J.* **245**, 56–64.

624 Assima G. P., Larachi F., Molson J. and Beaudoin G. (2014b) Emulation of ambient carbon  
625 dioxide diffusion and carbonation within nickel mining residues. *Miner. Eng.* **59**, 39–44.

626 Assima G. P., Larachi F., Molson J. and Beaudoin G. (2014c) Impact of temperature and  
627 oxygen availability on the dynamics of ambient CO<sub>2</sub> mineral sequestration by nickel  
628 mining residues. *Chem. Eng. J.* **240**, 394–403.

629 Ballirano P., De Vito C., Ferrini V. and Mignardi S. (2010) The thermal behaviour and  
630 structural stability of nesquehonite, MgCO<sub>3</sub>·3H<sub>2</sub>O, evaluated by in situ laboratory  
631 parallel-beam X-ray powder diffraction: New constraints on CO<sub>2</sub> sequestration within  
632 minerals. *J. Hazard. Mater.* **178**, 522–528.

633 Ballirano P., De Vito C., Mignardi S. and Ferrini V. (2013) Phase transitions in the Mg-CO<sub>2</sub>-  
634 H<sub>2</sub>O system and the thermal decomposition of dypingite, Mg<sub>5</sub>(CO<sub>3</sub>)<sub>4</sub>(OH)<sub>2</sub>·5H<sub>2</sub>O:  
635 Implications for geosequestration of carbon dioxide. *Chem. Geol.* **340**, 59–67.

636 Bea S.A., Wilson S.A., Mayer K. U., Dipple G. M., Power I. M. and Gamazo P. (2012)  
637 Reactive transport modeling of natural carbon sequestration in ultramafic mine tailings.  
638 *Vadose Zone J.* **11**.

639 Beinlich A. and Austrheim H. (2012) In situ sequestration of atmospheric CO<sub>2</sub> at low  
640 temperature and surface cracking of serpentinized peridotite in mine shafts. *Chem. Geol.*

641           **332–333**, 32–44.

642   Beinlich, A., Austrheim, H., Mavromatis, V., Grguric, B., Putnis, C.V., Putnis, A. (2018)

643           Peridotite weathering is the missing ingredient of Earth's continental crust composition.

644           *Nat. Commun.* **9**, 634.

645   Bénézech P., Berninger U.-N., Bovet N., Schott J. and Oelkers E. H. (2018) Experimental

646           determination of the solubility product of dolomite at 50 to 253°C. *Geochim.*

647           *Cosmochim. Acta* **224**, 262–275.

648   Bénézech P., Saldi G. D., Dandurand J. L. and Schott J. (2011) Experimental determination of

649           the solubility product of magnesite at 50 to 200°C. *Chem. Geol.* **286**, 21–31.

650   Berninger U.-N., Jordan G., Schott J. and Oelkers E. H. (2014) The experimental

651           determination of hydromagnesite precipitation rates at 22.5 - 75°C. *Mineral. Mag.* **78**,

652           1405–1416.

653   Boschi C., Dini A., Dallai L., Ruggieri G. and Gianelli G. (2009) Enhanced CO<sub>2</sub>-mineral

654           sequestration by cyclic hydraulic fracturing and Si-rich fluid infiltration into

655           serpentinites at Malenrata (Tuscany, Italy). *Chem. Geol.* **265**, 209–226.

656   Canterford J. H., Tsambourakis G. and Lambert B. (1984) Some observations on the

657           properties of dypingite , Mg<sub>5</sub>(CO<sub>3</sub>)<sub>4</sub>(OH)<sub>2</sub>·5H<sub>2</sub>O, and related minerals. *Mineral. Mag.*

658           **48**, 437–442.

659   Chaka A. M., Felmy A. R. and Qafoku O. (2016) Ab initio thermodynamics of magnesium

660           carbonates and hydrates in water-saturated supercritical CO<sub>2</sub> and CO<sub>2</sub>-rich regions.

661           *Chem. Geol.* **434**, 1–11.

662   Cheng W. and Li Z. (2010) Nucleation kinetics of nesquehonite (MgCO<sub>3</sub>·3H<sub>2</sub>O) in the

663           MgCl<sub>2</sub>-Na<sub>2</sub>CO<sub>3</sub> system. *J Cryst. Growth.* **312**, 1563–1571.

664   Cheng W. and Li Z. (2009) Precipitation of nesquehonite from homogeneous supersaturated

665           solutions. *Cryst. Res. Technol.* **44**, 937–947.

666 Cheng W., Li Z. and Demopoulos G. P. (2009) Effects of temperature on the preparation of  
667 magnesium carbonate hydrates by reaction of  $\text{MgCl}_2$  with  $\text{Na}_2\text{CO}_3$ . *Chinese J. Chem.*  
668 *Eng.* **17**, 661–666.

669 Davies P. J. and Bubela B. (1973) The transformation of nesquehonite into hydromagnesite.  
670 *Chem. Geol.* **12**, 289–300.

671 Ding W., Ouyang J. and Yang H. (2016) Synthesis and characterization of nesquehonite  
672 ( $\text{MgCO}_3 \cdot 3\text{H}_2\text{O}$ ) powders from natural talc. *Powder Technol.* **292**, 169–175.

673 Dong M., Cheng W., Li Z. and Demopoulos G. P. (2008) Solubility and stability of  
674 nesquehonite ( $\text{MgCO}_3 \cdot \text{H}_2\text{O}$ ) in mixed  $\text{NaCl} + \text{MgCl}_2$ ,  $\text{NH}_4\text{Cl} + \text{MgCl}_2$ ,  $\text{LiCl}$ , and  $\text{LiCl}$   
675  $+ \text{MgCl}_2$  solutions. *J. Chem. Eng. Data* **53**, 2586–2593.

676 Dong M., Li Z., Mi J. and Demopoulos G. P. (2009) Solubility and stability of nesquehonite  
677 ( $\text{MgCO}_3 \cdot 3\text{H}_2\text{O}$ ) in mixed  $\text{NaCl} + \text{MgCl}_2$ ,  $\text{NH}_4\text{Cl} + \text{MgCl}_2$ ,  $\text{LiCl}$ , and  $\text{LiCl} + \text{MgCl}_2$   
678 solutions. *J. Chem. Eng. Data* **54**, 3002–3007.

679 Falk E. S., Guo W., Paukert A. N., Matter J. M., Mervine E. M. and Kelemen P. B. (2016)  
680 Controls on the stable isotope compositions of travertine from hyperalkaline springs in  
681 Oman: Insights from clumped isotope measurements. *Geochim. Cosmochim. Acta* **192**,  
682 1–28.

683 Felmy A. R., Qafoku O., Arey B. W., Hu J. Z., Hu M., Todd Schaefer H., Ilton E. S., Hess N.  
684 J., Pearce C. I., Feng J. and Rosso K. M. (2012) Reaction of water-saturated  
685 supercritical  $\text{CO}_2$  with forsterite: Evidence for magnesite formation at low temperatures.  
686 *Geochim. Cosmochim. Acta* **91**, 271–282.

687 Frost R. L., Bahfenne S., Graham J. and Martens W. N. (2008) Thermal stability of artinite,  
688 dypingite and brugnatellite—Implications for the geosequestration of green house gases.  
689 *Thermochim. Acta* **475**, 39–43.

690 Frost R. L. and Palmer S. J. (2011) Infrared and infrared emission spectroscopy of

691 nesquehonite  $\text{Mg}(\text{OH})(\text{HCO}_3) \cdot 2\text{H}_2\text{O}$ -implications for the formula of nesquehonite.  
692 *Spectrochim. Acta - Part A Mol. Biomol. Spectrosc.* **78**, 1255–1260.

693 Garcia del Real P. G., Maher K., Kluge T., Bird D. K., Brown G. E. and John C. M. (2016)  
694 Clumped-isotope thermometry of magnesium carbonates in ultramafic rocks. *Geochim.*  
695 *Cosmochim. Acta.* **193**, 222–250.

696 Gautier Q., Bénézech P., Mavromatis V. and Schott J. (2014) Hydromagnesite solubility  
697 product and growth kinetics in aqueous solution from 25 to 75°C. *Geochim.*  
698 *Cosmochim. Acta* **138**, 1–20.

699 Gerdemann S. J., O'Connor W. K., Dahlin D. C., Penner L. R. and Rush H. (2007) Ex situ  
700 aqueous mineral carbonation. *Environ. Sci. Technol.* **41**, 2587–2593.

701 Gislason S. R. and Oelkers E. H. (2014) Carbon storage in basalt. *Science* **344**, 373–374.

702 Gras A., Beaudoin G., Molson J., Plante B., Bussière B., Lemieux J. M. and Dupont P. P.  
703 (2017) Isotopic evidence of passive mineral carbonation in mine wastes from the  
704 Dumont Nickel Project (Abitibi, Quebec). *Int. J. Greenhouse Gas Control* **60**, 10–23.

705 Hales M., Frost R. and Martens W. (2008) Thermo-Raman spectroscopy of synthetic  
706 nesquehonite - implication for the geosequestration of greenhouse gases. *J. Raman*  
707 *Spectrosc.* **38**, 1141–1149.

708 Hamilton J. L., Wilson S. A., Morgan B., Turvey C. C., Paterson D. J., Jowitt S. M.,  
709 McCutcheon J. and Southam G. (2018) Fate of transition metals during passive  
710 carbonation of ultramafic mine tailings via air capture with potential for metal resource  
711 recovery. *Int. J. Greenhouse Gas Control* **71**, 155–167.

712 Hamilton J. L., Wilson S. A., Morgan B., Turvey C. C., Paterson D. J., MacRae C.,  
713 McCutcheon J. and Southam G. (2016) Nesquehonite sequesters transition metals and  
714  $\text{CO}_2$  during accelerated carbon mineralisation. *Int. J. Greenhouse Gas Control.* **55**, 73–  
715 81.

716 Hänchen M., Prigiobbe V., Baciocchi R. and Mazzotti M. (2008) Precipitation in the Mg-  
717 carbonate system—effects of temperature and CO<sub>2</sub> pressure. *Chem. Eng. Sci.* **63**, 1012–  
718 1028.

719 Harrison A. L., Dipple G. M., Power I. M. and Mayer K. U. (2016) The impact of evolving  
720 mineral-water-gas interfacial areas on mineral-fluid reaction rates in unsaturated porous  
721 media. *Chem. Geol.* **421**, 65–80.

722 Harrison A. L., Dipple G. M., Power I. M. and Mayer K. U. (2015) Influence of surface  
723 passivation and water content on mineral reactions in unsaturated porous media:  
724 Implications for brucite carbonation and CO<sub>2</sub> sequestration. *Geochim. Cosmochim. Acta*  
725 **148**, 477–495.

726 Harrison A. L., Dipple G. M., Song W., Power I. M., Mayer K. U., Beinlich A. and Sinton D.  
727 (2017) Changes in mineral reactivity driven by pore fluid mobility in partially wetted  
728 porous media. *Chem. Geol.* **463**, 1–11.

729 Harrison A. L., Power I. M. and Dipple G. M. (2013a) Accelerated carbonation of brucite in  
730 mine tailings for carbon sequestration. *Environ. Sci. Technol.* **47**, 126–134.

731 Harrison A. L., Power I. M. and Dipple G. M. (2013b) Strategies for enhancing carbon  
732 sequestration in Mg-rich mine tailings. In *Reliable Mine Water Technology (Vol. 1)* (eds.  
733 A. Brown, L. Figueroa, and C. Wolkersdorfer). Publication Printers, Denver, Colorado,  
734 USA. pp. 593–598.

735 Hartmann J., West J., Renforth P., Kohler P., De La Rocha C., Wolf-Gladrow D. A., Durr H.  
736 and Scheffran J. (2013) Enhanced chemical weathering as a geoengineering strategy to  
737 reduce atmospheric carbon dioxide, a nutrient source and to mitigate ocean acidification.  
738 *Rev. Geophys.* **51**, 113–149.

739 Helgeson H. C. (1969) Thermodynamics of hydrothermal systems at elevated temperatures  
740 and pressures. *Am. J. Sci.* **267**, 729–804.



741 Highfield J., Chen J., Haghughatlari M., Abacka J. and Zevenhoven R. (2016) Low-  
742 temperature gas-solid carbonation of magnesia and magnesium hydroxide promoted by  
743 non-immersive contact with water. *R. Soc. Chem. Adv.* **6**, 89655–89664.

744 Hopkinson L., Kristova P., Rutt K. and Cressey G. (2012) Phase transitions in the system  
745 MgO – CO<sub>2</sub> – H<sub>2</sub>O during CO<sub>2</sub> degassing of Mg-bearing solutions. *Geochim.*  
746 *Cosmochim. Acta* **76**, 1–13.

747 Hopkinson L., Rutt K. and Cressey G. (2008) The transformation of nesquehonite to  
748 hydromagnesite in the system CaO-MgO-H<sub>2</sub>O-CO<sub>2</sub>: An experimental spectroscopic  
749 study. *J. Geol.* **116**, 387–400.

750 Hostetler P. (1964) The degree of saturation of magnesium and calcium carbonate minerals in  
751 natural waters. *Int. Assoc. Sci. Hydrol.* **64**, 34–49.

752 Hövelmann J., Putnis C. V, Ruiz-Agudo E. and Austrheim H. (2012) Direct nanoscale  
753 observations of CO<sub>2</sub> sequestration during brucite [Mg(OH)<sub>2</sub>] dissolution. *Environ. Sci.*  
754 *Technol.* **46**, 5253–5260.

755 Jauffret G., Morrison J. and Glasser F. P. (2015) On the thermal decomposition of  
756 nesquehonite. *J. Therm. Anal. Calorim.*, 5–10.

757 Kazakov A. V., Tikhomirova M. M. and Plotnikova V. I. (1959) The system of carbonate  
758 equilibria. *Int. Geol. Rev.* **1**, 1–39.

759 Kelemen P. B. and Matter J. (2008) In situ carbonation of peridotite for CO<sub>2</sub> storage. *Proc.*  
760 *Natl. Acad. Sci.* **105**, 17295–17300.

761 Kline W. (1929) The solubility of magnesium carbonate (nesquehonite) in water at 25° and  
762 pressures of carbon dioxide up to one atmosphere. *J. Am. Chem. Soc.* **51**, 2093–2097.

763 Königsberger E., Königsberger L.-C. and Gamsjäger H. (1999) Low-temperature  
764 thermodynamic model for the system Na<sub>2</sub>CO<sub>3</sub>-MgCO<sub>3</sub>-CaCO<sub>3</sub>-H<sub>2</sub>O. *Geochim.*  
765 *Cosmochim. Acta* **63**, 3105–3119.

- 766 Kristova P., Hopkinson L. J., Rutt K. J., Hunter H. M. A. and Cressey G. (2014) Carbonate  
767 mineral paragenesis and reaction kinetics in the system MgO–CaO–CO<sub>2</sub>–H<sub>2</sub>O in  
768 presence of chloride or nitrate ions at near surface ambient temperatures. *Appl.*  
769 *Geochemistry* **50**, 16–24.
- 770 Lackner K. S. (2003) A Guide to CO<sub>2</sub> Sequestration. *Science* **300**, 1677–1678.
- 771 Lackner K. S., Wendt C. H., Butt D. P., Joyce E. L. and Sharp D. H. (1995) Carbon dioxide  
772 disposal in carbonate minerals. *Energy* **20**, 1153–1170.
- 773 Lanas J. and Alvarez J. I. (2004) Dolomitic lime: Thermal decomposition of nesquehonite.  
774 *Thermochim. Acta* **421**, 123–132.
- 775 Langmuir D. (1965) Stability of carbonates in the system MgO–CO<sub>2</sub>–H<sub>2</sub>O. *J. Geol.* **73**, 730–  
776 754.
- 777 Lin Y., Zheng M. and Ye C. (2017) Hydromagnesite precipitation in the alkaline lake Dujiali,  
778 central Qinghai-Tibetan Plateau: Constraints on hydromagnesite precipitation from  
779 hydrochemistry and stable isotopes. *Appl. Geochem.* **78**, 139–148.
- 780 Loring J. S., Thompson C. J., Zhang C., Wang Z., Schaef H. T. and Rosso K. M. (2012) In  
781 situ infrared spectroscopic study of brucite carbonation in dry to water-saturated  
782 supercritical carbon dioxide. *J. Phys. Chem. A* **116**, 4768–4777.
- 783 Marion G. (2001) Carbonate mineral solubility at low temperatures in the Na–K–Mg–Ca–H–  
784 Cl–SO<sub>4</sub>–OH–HCO<sub>3</sub>–CO<sub>3</sub>–CO<sub>2</sub>–H<sub>2</sub>O system. *Geochim. Cosmochim. Acta* **65**, 1883–1896.
- 785 Matter J., Stute M., Snæbjörnsdóttir S. Ó., Oelkers E., Gislason S. R., Aradóttir E. S.,  
786 Sigfusson B., Gunnarsson I., Alfredsson H. A., Wolff-boenisch D., Mesfin K.,  
787 Fernandez de la Reguera Taya D., Hall J., Dideriksen K. and Broecker W. S. (2016)  
788 Rapid carbon mineralization for permanent disposal of anthropogenic carbon dioxide  
789 emissions. *Science* **352**, 1312–1314.
- 790 Mavromatis, V., Bundeleva, I.A., Shirokova, L.S., Millo, C., Pokrovsky, O.S., Bénézech, P.,

791 Ader, M., Oelkers, E.H. (2015) The continuous re-equilibration of carbon isotope  
792 compositions of hydrous Mg carbonates in the presence of cyanobacteria. *Chem. Geol.*  
793 **404**, 41-51.

794 Mavromatis V., Pearce C. R., Shirokova L. S., Bundeleva I. A., Pokrovsky O. S., Bénézech P.  
795 and Oelkers E. H. (2012) Magnesium isotope fractionation during hydrous magnesium  
796 carbonate precipitation with and without cyanobacteria. *Geochim. Cosmochim. Acta* **76**,  
797 161–174.

798 McClain C. N. and Maher K. (2016) Chromium fluxes and speciation in ultramafic  
799 catchments and global rivers. *Chem. Geol.* **426**, 135–157.

800 McCutcheon J., Power I. M., Harrison A. L., Dipple G. M. and Southam G. (2014) A  
801 greenhouse-scale photosynthetic microbial bioreactor for carbon sequestration in  
802 magnesium carbonate minerals. *Environ. Sci. Technol.* **48**, 9142–9151.

803 McCutcheon J., Turvey C. C., Wilson S.A., Hamilton J. L. and Southam G. (2017)  
804 Experimental deployment of microbial mineral carbonation at an asbestos mine:  
805 Potential applications to carbon storage and tailings stabilization. *Minerals* **7**, 15–18.

806 McCutcheon J., Wilson S. A. and Southam G. (2016) Microbially accelerated carbonate  
807 mineral precipitation as a strategy for in situ carbon sequestration and rehabilitation of  
808 asbestos mine sites. *Environ. Sci. Technol.*, **50**, 1419–1423.

809 Mervine E. M., Humphris S. E., Sims K. W. W., Kelemen P. B. and Jenkins W. J. (2014)  
810 Carbonation rates of peridotite in the Samail Ophiolite, Sultanate of Oman, constrained  
811 through <sup>14</sup>C dating and stable isotopes. *Geochim. Cosmochim. Acta* **126**, 371–397.

812 Montes-Hernandez G., Renard F., Chiriack R., Findling N. and Toche F. (2012) Rapid  
813 precipitation of magnesite microcrystals from Mg(OH)<sub>2</sub> - H<sub>2</sub>O - CO<sub>2</sub> slurry enhanced by  
814 NaOH and a heat-aging step (from ~20 to 90 °C). *Cryst. Growth Des.* **12**, 5233–5240.

815 Montserrat F., Renforth P., Hartmann J., Knops P., Leermakers M. and Meysman F. J. R.

816 (2017) Olivine dissolution in seawater: Implications for CO<sub>2</sub> sequestration through  
817 Enhanced Weathering in coastal environments. *Environ. Sci. Technol.* **51**, 3960–3972.

818 Morgan B., Wilson S. A., Madsen I. C., Gozukara Y. M. and Habsuda J. (2015) Increased  
819 thermal stability of nesquehonite (MgCO<sub>3</sub>·3H<sub>2</sub>O) in the presence of humidity and CO<sub>2</sub>:  
820 Implications for low-temperature CO<sub>2</sub> storage. *Int. J. Greenhouse Gas Control* **39**, 366–  
821 376.

822 Oelkers, E.H., Berninger, U.N., Perez-Fernandez, A., Chmeleff, J., Mavromatis, V. (2018)  
823 The temporal evolution of magnesium isotope fractionation during hydromagnesite  
824 dissolution, precipitation, and at equilibrium. *Geochim. Cosmochim. Acta* **226**, 36-49.

825 Oelkers E. H. and Cole D. R. (2008) Carbon dioxide sequestration: A solution to a global  
826 problem. *Elements* **4**, 305–310.

827 Oskierski H. C., Dlugogorski B. Z. and Jacobsen G. (2013) Sequestration of atmospheric CO<sub>2</sub>  
828 in chrysotile mine tailings of the Woodsreef Asbestos Mine, Australia: Quantitative  
829 mineralogy, isotopic fingerprinting and carbonation rates. *Chem. Geol.* **358**, 156–169.

830 Oskierski H. C., Dlugogorski B. Z., Oliver T. K. and Jacobsen G. (2016) Chemical and  
831 isotopic signatures of waters associated with the carbonation of ultramafic mine tailings,  
832 Woodsreef Asbestos Mine, Australia. *Chem. Geol.* **436**, 11–23.

833 Palmer D. A. and Wesolowski D. J. (1997) Potentiometric measurements of the first  
834 hydrolysis quotient of magnesium (II) to 250°C and 5 molal ionic strength ( NaCl ). *J.*  
835 *Solution Chem.* **26**, 2167–232.

836 Parkhurst D. L. and Appelo C. A. J. (2013) Description of Input and Examples for  
837 PHREEQC Version 3 — A Computer Program for Speciation , Batch-Reaction , One-  
838 Dimensional Transport , and Inverse Geochemical Calculations. In *U.S. Geological*  
839 *Survey Techniques and Methods, book 6, chap. A43, 497 p.* Denver, Colorado. p. 497.

840 Patterson C. S., Busey R. H. and Mesmer R. E. (1984) Second ionization of carbonic acid in

841 NaCl media to 250°C. *J. Solution Chem.* **13**, 647–661.

842 Patterson C. S., Slocum G. H., Busey R. H. and Mesmer R. E. (1982) Carbonate equilibria in  
843 hydrothermal systems: First ionization of carbonic acid in NaCl media to 300°C.  
844 *Geochim. Cosmochim. Acta* **46**, 1653–1663.

845 Power I. M., Dipple G. M. and Southam G. (2010) Bioleaching of ultramafic tailings by  
846 *Acidithiobacillus* spp. for CO<sub>2</sub> sequestration. *Environ. Sci. Technol.* **44**, 456–462.

847 Power I. M., Harrison A. L. and Dipple G. M. (2016) Accelerating mineral carbonation using  
848 carbonic anhydrase. *Environ. Sci. Technol.* **50**, 2610–2618.

849 Power I. M., Harrison A. L., Dipple G. M. and Southam G. (2013c) Carbon sequestration via  
850 carbonic anhydrase facilitated magnesium carbonate precipitation. *Int. J. Greenhouse*  
851 *Gas Control* **16**, 145–155.

852 Power I. M., Harrison A. L., Dipple G. M., Wilson S. A., Kelemen P. B., Hitch M. and  
853 Southam G. (2013a) Carbon mineralization: From natural analogues to engineered  
854 systems. *Rev. Mineral. Geochemistry* **77**, 305–360.

855 Power I. M., Kenward P. A., Dipple G. M. and Raudsepp M. (2017) Room temperature  
856 magnesite precipitation. *Cryst. Growth Des.* **17**, 5652–5659.

857 Power I. M., McCutcheon J., Harrison A. L., Wilson S. A., Dipple G. M., Kelly S., Southam  
858 C. and Southam G. (2014a) Strategizing carbon-neutral mines: A Case for pilot projects.  
859 *Minerals* **4**, 399–436.

860 Power I. M., Wilson S. A. and Dipple G. M. (2013b) Serpentinite carbonation for CO<sub>2</sub>  
861 sequestration. *Elements* **9**, 115–121.

862 Power I. M., Wilson S. A., Harrison A. L., Dipple G. M., McCutcheon J., Southam G. and  
863 Kenward P. A. (2014b) A depositional model for hydromagnesite-magnesite playas near  
864 Atlin, British Columbia, Canada. *Sedimentology* **61**, 1701–1733.

865 Power I. M., Wilson S. A., Thom J. M., Dipple G. M., Gabites J. E. and Southam G. (2009)

866 The hydromagnesite playas of Atlin, British Columbia, Canada: A biogeochemical  
867 model for CO<sub>2</sub> sequestration. *Chem. Geol.* **260**, 286–300.

868 Power I. M., Wilson S. A., Thom J. M., Dipple G. M. and Southam G. (2007) Biologically  
869 induced mineralization of dypingite by cyanobacteria from an alkaline wetland near  
870 Atlin, British Columbia, Canada. *Geochem. Trans.* **8**, 13.

871 Pronost J., Beaudoin G., Lemieux J.-M., Hebert R., Constantin M., Marcouiller S., Klein M.,  
872 Duchesne J., Molson J. W., Larachi F. and Maldague X. (2012) CO<sub>2</sub>-depleted warm air  
873 venting from chrysotile milling waste (Thetford Mines, Canada): Evidence for in-situ  
874 carbon capture from the atmosphere. *Geology* **40**, 275–278.

875 Pronost J., Beaudoin G., Tremblay J., Larachi F., Duchesne J., Hébert R. and Constantin M.  
876 (2011) Carbon sequestration kinetic and storage capacity of ultramafic mining waste.  
877 *Environ. Sci. Technol.* **45**, 9413–9420.

878 Raade G. (1970) Dypingite, a new hydrous basic carbonate of magnesium, from Norway.  
879 *Am. Mineral.* **55**, 1457–1465.

880 Renforth P. (2012) The potential of enhanced weathering in the UK. *Int. J. Greenhouse Gas*  
881 *Control* **10**, 229–243.

882 Rigopoulos I., Harrison A. L., Delimitis A., Ioannou I., Efstathiou A. M., Kyratsi T. and  
883 Oelkers E. H. (2018) Carbon sequestration via enhanced weathering of peridotites and  
884 basalts in seawater. *Appl. Geochem.* **91**, 197–207.

885 Robie R. A. and Hemingway B. S. (1972) The heat capacities at low-temperatures and  
886 entropies at 298.15 K of nesquehonite, MgCO<sub>3</sub>·3H<sub>2</sub>O, and hydromagnesite. *Am.*  
887 *Mineral.* **57**, 1768–1781.

888 Robie R. and Hemingway B. (1973) The enthalpies of formation of nesquehonite,  
889 MgCO<sub>3</sub>·3H<sub>2</sub>O, and hydromagnesite, 5MgO·4CO<sub>2</sub>·5H<sub>2</sub>O. *J. Res. U.S. Geol. Surv.* **1**,  
890 543–547.

891 Ruiz-Agudo E., Putnis C. V., Rodriguez-Navarro C. and Putnis A. (2012) Mechanism of  
892 leached layer formation during chemical weathering of silicate minerals. *Geology* **40**,  
893 947–950.

894 Saldi G. D., Jordan G., Schott J. and Oelkers E. H. (2009) Magnesite growth rates as a  
895 function of temperature and saturation state. *Geochim. Cosmochim. Acta* **73**, 5646–5657.

896 Saldi G. D., Schott J., Pokrovsky O. S., Gautier Q. and Oelkers E. H. (2012) An experimental  
897 study of magnesite precipitation rates at neutral to alkaline conditions and 100–200°C as  
898 a function of pH, aqueous solution composition and chemical affinity. *Geochim.*  
899 *Cosmochim. Acta* **83**, 93–109.

900 Schaef H. T., Mcgrail B. P., Loring J. L., Bowden M. E., Arey B. W. and Rosso K. M. (2013)  
901 Forsterite [Mg<sub>2</sub>SiO<sub>4</sub>] carbonation in wet supercritical CO<sub>2</sub>: An in situ high-pressure X-  
902 ray diffraction study. *Environ. Sci. Technol.* **47**, 174–181.

903 Schaef H. T., Windisch C. F., McGrail B. P., Martin P. F. and Rosso K. M. (2011) Brucite  
904 [Mg(OH)<sub>2</sub>] carbonation in wet supercritical CO<sub>2</sub>: An in situ high pressure X-ray  
905 diffraction study. *Geochim. Cosmochim. Acta* **75**, 7458–7471.

906 Schuiling R. D. and Boer P. L. De (2010) Coastal spreading of olivine to control atmospheric  
907 CO<sub>2</sub> concentrations: A critical analysis of viability. Comment: Nature and laboratory  
908 models are different. *Int. J. Greenhouse Gas Control* **4**, 855–856.

909 Shirokova L. S., Mavromatis V., Bundeleva I. A., Pokrovsky O. S., Bénézech P., Gérard E.,  
910 Pearce C. R. and Oelkers E. H. (2013) Using Mg isotopes to trace cyanobacterially  
911 mediated magnesium carbonate precipitation in alkaline lakes. *Aquat. Geochemistry* **19**,  
912 1–24.

913 Shock E. L. and Helgeson H. C. (1988) Calculation of the thermodynamic and transport  
914 properties of aqueous species at high pressures and temperatures: Correlation algorithms  
915 for ionic species and equation of state predictions to 5 kb and 1000°C. *Geochim.*

916 *Cosmochim. Acta* **52**, 2009–2036.

917 Shock E. L., Sassani D. C., Willis M. and Sverjensky D. A. (1997) Inorganic species in  
918 geologic fluids: Correlations among standard molal thermodynamic properties of  
919 aqueous ions and hydroxide complexes. *Geochim. Cosmochim. Acta* **61**, 907–950.

920 Stefansson A., Bénézech P., and Schott J. (2014) Potentiometric and spectrophotometric  
921 study of the stability of magnesium carbonate and bicarbonate pairs to 150C and  
922 aqueous inorganic carbon speciation and magnesite solubility. *Geochim. Cosmochim.*  
923 *Acta* **138**, 21–31.

924 Sundquist E. T. (1993) The global carbon dioxide budget. *Science*. **259**, 934–941.

925 Sutradhar N., Sinhamahapatra A., Pahari S. K., Pal P., Bajaj H. C., Mukhopadhyay I. and  
926 Panda A. B. (2011) Controlled synthesis of different morphologies of MgO and their use  
927 as solid base catalysts. *J. Phys. Chem. C* **115**, 12308–12316.

928 Vágvölgyi V., Hales M., Frost R. L., Locke A., Kristóf J. and Horváth E. (2008)  
929 Conventional and controlled rate thermal analysis of nesquehonite  $\text{Mg}(\text{HCO}_3)(\text{OH}) \cdot 2$   
930  $(\text{H}_2\text{O})$ . *J. Therm. Anal. Calorim.* **94**, 523–528.

931 Wagman D. D., Evans W. H., Parker V. B., Schumm R. H., Halow I., Bailey S. M., Churney  
932 K. L. and Nuttall R. L. (1982) The NBS tables of chemical thermodynamic properties:  
933 selected values for inorganic and C1 and C2 organic substances in SI units. *J. Chem.*  
934 *Ref. Data*, 392, 11(supplement n. 2).

935 Wang D. and Li Z. (2012) Chemical modeling of nesquehonite solubility in Li + Na + K +  
936  $\text{NH}_4$  + Mg + Cl +  $\text{H}_2\text{O}$  System with a speciation-based approach. *Chinese J. Chem. Eng.*  
937 **20**, 2670276.

938 Wang Y., Li Z. and Demopoulos G. P. (2008) Controlled precipitation of nesquehonite  
939  $(\text{MgCO}_3 \cdot 3\text{H}_2\text{O})$  by the reaction of  $\text{MgCl}_2$  with  $(\text{NH}_4)_2\text{CO}_3$ . **310**, 1220–1227.

940 Wilson S. A., Barker S. L. L., Dipple G. M. and Atudorei V. (2010) Isotopic disequilibrium



941 during uptake of atmospheric CO<sub>2</sub> into mine process waters: Implications for CO<sub>2</sub>  
942 sequestration. *Environ. Sci. Technol.* **44**, 9522–9529.

943 Wilson S. A., Dipple G. M., Power I. M., Barker S. L. L., Fallon S. J. and Southam G. (2011)  
944 Subarctic weathering of mineral wastes provides a sink for atmospheric CO<sub>2</sub>. *Environ.*  
945 *Sci. Technol.* **45**, 7727–7736.

946 Wilson S. A., Dipple G. M., Power I. M., Thom J. M., Anderson R. G., Raudsepp M.,  
947 Gabites J. E. and Southam G. (2009) Carbon dioxide fixation within mine wastes of  
948 ultramafic-hosted ore deposits: Examples from the Clinton Creek and Cassiar chrysotile  
949 deposits, Canada. *Econ. Geol.* **104**, 95–112.

950 Wilson S. A., Harrison A. L., Dipple G. M., Power I. M., Barker S. L. L., Mayer K. U.,  
951 Fallon S. J., Raudsepp M. and Southam G. (2014) Offsetting of CO<sub>2</sub> emissions by air  
952 capture in mine tailings at the Mount Keith Nickel Mine, Western Australia: Rates,  
953 controls and prospects for carbon neutral mining. *Int. J. Greenhouse Gas Control* **25**,  
954 121–140.

955 Wilson S. A., Raudsepp M. and Dipple G. M. (2009) Quantifying carbon fixation in trace  
956 minerals from processed kimberlite: A comparative study of quantitative methods using  
957 X-ray powder diffraction data with applications to the Diavik Diamond Mine, Northwest  
958 Territories, Canada. *Appl. Geochem.* **24**, 2312–2331.

959 Wilson S. A., Raudsepp M. and Dipple G. M. (2006) Verifying and quantifying carbon  
960 fixation in minerals from serpentine-rich mine tailings using the Rietveld method with  
961 X-ray powder diffraction data. *Am. Mineral.* **91**, 1331–1341.

962 Xiong Y. (2011) Experimental determination of solubility constant of hydromagnesite (5424)  
963 in NaCl solutions up to 4.4 m at room temperature. *Chem. Geol.* **284**, 262–269.

964 Xiong Y. and Lord A. S. (2008) Experimental investigations of the reaction path in the  
965 MgO–CO<sub>2</sub>–H<sub>2</sub>O system in solutions with various ionic strengths, and their applications

966 to nuclear waste isolation. *Appl. Geochem.* **23**, 1634–1659.

967 Zhang Z., Zheng Y., Ni Y., Liu Z., Chen J. and Liang X. (2006) Temperature- and pH-  
968 dependent morphology and FT-IR analysis of magnesium carbonate hydrates. *J. Phys.*  
969 *Chem. B* **110**, 12969–12973.

970 Zhao L., Sang L., Chen J., Ji J. and Teng H. H. (2010) Aqueous carbonation of natural  
971 brucite: Relevance to CO<sub>2</sub> sequestration. *Environ. Sci. Technol.* **44**, 406–411.

972 Zhao L., Zhu C., Ji J., Chen J. and Teng H. H. (2013) Thermodynamic and kinetic effect of  
973 organic solvent on the nucleation of nesquehonite. **106**, 192–202.

974

975 **Tables**

976 Table 1. Aqueous composition, aqueous activities, and mineralogical composition measured

977 over time for all experiments.

Experiment	Time (h) <sup>a</sup>	pH (±0.03)	Alkalinity (× 10 <sup>-2</sup> mol/L; ±0.36 × 10 <sup>-2</sup> )	DIC <sup>b</sup> (× 10 <sup>-2</sup> mol/L; ±0.36 × 10 <sup>-2</sup> )	Mg (× 10 <sup>-2</sup> mol/L)	Mg error (3σ × 10 <sup>-2</sup> )	a <sub>Mg2+</sub> <sup>c</sup> (× 10 <sup>-3</sup> )	a <sub>CO32-</sub> <sup>c</sup> (× 10 <sup>-3</sup> )	a <sub>H2O</sub> <sup>c</sup>	Mineralogy <sup>d</sup>
5	0	8.25	5.95	6.00				0.19	0.995	nsq
	6	9.44	9.04	7.54	1.214	0.005	2.431	2.88	0.994	nsq
	9	9.40	8.90	7.54	1.157	0.004	2.381	2.65	0.994	nsq
	12	9.41	8.94	7.49	1.290	0.012	2.641	2.71	0.994	nsq
	24	9.39	9.17	7.75	1.269	0.010	2.586	2.70	0.994	nsq
	49	9.43	9.16	7.65	1.278	0.017	2.558	2.87	0.994	nsq
	120 (nsq)	9.47	9.66	7.91	1.510	0.006	2.915	3.15	0.994	nsq
	367 (nsq)	9.59	9.71	7.66	1.505	0.006	2.734	3.76	0.994	nsq
	1085 (nsq)	9.39	9.68	8.14	1.498	0.016	3.001	2.78	0.994	nsq
	1420 (nsq)	9.59	9.67	7.62	1.502	0.014	2.732	3.75	0.994	nsq
25_short	0	8.15	5.94	5.97				0.25	0.995	nsq
	4	9.20	8.99	7.52	1.167	0.015	1.976	2.85	0.994	nsq
	6	9.20	8.99	7.55	1.094	0.011	1.847	2.86	0.994	nsq
	8	9.19	8.87	7.47	1.119	0.003	1.926	2.75	0.994	nsq
	10	9.18	8.61	7.27	1.075	0.019	1.882	2.67	0.994	nsq
	12	9.20	8.72	7.31	1.114	0.008	1.920	2.76	0.994	nsq
	24 (nsq)	9.19	8.95	7.50	1.197	0.013	2.048	2.79	0.994	nsq
	49 (nsq)	9.19	8.97	7.52	1.183	0.002	2.022	2.79	0.994	nsq
	120 (nsq)	9.20	9.02	7.54	1.192	0.011	2.019	2.85	0.994	nsq
	367 (nsq)	9.19	9.05	7.59	1.216	0.015	2.076	2.79	0.994	nsq
	1086	8.97	8.99	8.00	1.113	0.006	2.158	1.95	0.994	nsq+dyp
25_long	0	8.23	5.92	5.92	0.006	0.001	0.002	0.30	0.995	nsq
	22 (nsq)	9.27	8.68	7.12	1.105	0.011	1.821	3.08	0.994	nsq (minor dyp)
	122 (nsq)	9.23	8.69	7.23	1.098	0.009	1.861	2.88	0.994	nsq
	359	8.94	8.69	7.77	1.119	0.012	2.249	1.78	0.994	nsq+dyp
	599	8.82	8.66	7.95	1.075	0.001	2.296	1.42	0.994	nsq+dyp
	843	8.88	8.69	7.87	1.104	0.007	2.288	1.59	0.994	nsq+dyp
	987	8.86	8.09	7.38	1.011	0.020	2.187	1.43	0.994	nsq+dyp
	1157	8.82	8.49	7.80	1.065	0.012	2.303	1.38	0.994	dyp+nsq
	1367 (dyp)	8.81	8.49	7.81	1.069	0.010	2.325	1.35	0.994	dyp+dyp-like
	1607 (dyp)	8.81	8.61	7.93	1.051	0.062	2.265	1.38	0.994	dyp+dyp-like
	2043 (dyp)	8.90	8.49	7.68	1.036	0.008	2.148	1.62	0.994	dyp+dyp-like

978

979

980 Table 1 (continued). Aqueous composition, aqueous activities, and mineralogical  
 981 composition measured over time for all experiments.

Experiment	Time (h) <sup>a</sup>	pH (±0.03)	Alkalinity (× 10 <sup>-2</sup> mol/L; ±0.36 × 10 <sup>-2</sup> )	DIC <sup>b</sup> (× 10 <sup>-2</sup> mol/L; ±0.36 × 10 <sup>-2</sup> )	Mg (× 10 <sup>-2</sup> mol/L)	Mg error (3σ × 10 <sup>-2</sup> )	a <sub>Mg2+</sub> <sup>c</sup> (× 10 <sup>-3</sup> )	a <sub>CO32-</sub> <sup>c</sup> (× 10 <sup>-3</sup> )	a <sub>H2O</sub> <sup>c</sup>	Mineralogy <sup>d</sup>
35_short	0	8.11	5.94	5.96	0.004	nd <sup>e</sup>	0.001	0.28	0.995	nsq
	3 (nsq)	9.12	8.77	7.35	1.051	0.008	1.629	2.82	0.994	nsq
	5 (nsq)	9.12	8.64	7.24	1.063	0.018	1.670	2.75	0.994	nsq
	7 (nsq)	9.14	8.63	7.21	1.047	0.015	1.625	2.83	0.994	nsq
	11 (nsq)	9.11	8.65	7.27	1.050	0.016	1.654	2.73	0.994	nsq
	24 (nsq)	9.22	8.74	7.11	1.048	0.010	1.519	3.26	0.994	nsq
	75	9.19	8.75	7.18	1.062	0.004	1.573	3.12	0.994	nsq (trace dyp)
	122	9.12	8.74	7.33	1.054	0.007	1.647	2.78	0.994	nsq+dyp
	191	9.04	8.78	7.52	1.080	0.008	1.778	2.45	0.994	nsq+dyp
	243	9.02	8.65	7.46	1.048	0.011	1.767	2.32	0.994	nsq+dyp
432	8.84	8.43	7.61	0.900	0.004	1.705	1.70	0.994	dyp+nsq	
35_long	0	8.08	5.93	5.96	0.001	0.0001	0.004	0.26	0.995	nsq
	26 (nsq)	9.17	8.54	7.06	1.044	0.002	1.596	2.95	0.994	nsq
	74 (nsq)	9.20	8.57	7.02	1.056	0.009	1.577	3.10	0.994	nsq
	123	9.09	8.60	7.26	1.057	0.015	1.697	2.64	0.994	nsq (trace dyp)
	244	8.90	8.66	7.66	1.138	0.011	2.082	1.89	0.994	nsq+dyp
	311	8.80	8.14	7.37	1.048	0.002	2.087	1.50	0.994	dyp+nsq
	482 (dyp)	8.65	8.36	7.80	0.951	0.007	2.018	1.16	0.994	dyp
	552 (dyp)	8.64	7.58	7.09	0.922	0.009	2.057	1.03	0.994	dyp
	600 (dyp)	8.63	8.29	7.77	0.930	0.007	1.999	1.10	0.994	dyp
	718	8.63	8.18	7.67	0.915	0.007	1.977	1.10	0.994	dyp+ unknown phase

982 <sup>a</sup>(nsq) indicates time points used for the calculation of  $K_{sp}^{nsq}$ , and (dyp) indicates timepoints used for the calculation of  $K_{sp}^{dyp}$

983 <sup>b</sup>DIC = dissolved inorganic carbon; calculated using PHREEQC V3

984 <sup>c</sup>Aqueous activity calculated using PHREEQC V3

985 <sup>d</sup>determined with X-ray diffraction

986 <sup>e</sup>No data

987

988

989

990

991

992

993 Table 2. Solubility products for nesquehonite and dypingite from this study and previous  
 994 works including the PHREEQC databases.

Temperature (°C)	<i>Nesquehonite log K<sub>sp</sub><sup>nsq</sup></i>							<i>Dypingite log K<sub>sp</sub><sup>dyp</sup></i>		
	<i>this study</i> ±3σ	PHREEQC		<i>Wang and Li</i> (2012)	<i>Kline</i> (1929)	<i>Langmuir</i> (1965)	<i>Hostetler</i> (1964)	<i>this study</i>		
		<i>Minteqv4</i>	<i>LLNL</i>					<i>a<sub>H2O</sub>=1</i> ±3σ	<i>8H<sub>2</sub>O</i> ±3σ	<i>5H<sub>2</sub>O</i> ±3σ
5	-5.03±0.13	-4.36	-4.53	-4.99						
25	-5.27±0.15	-4.67	-5.06	-5.27	-4.96	-5.59±0.1 -5.42*	-5.51	-34.93±0.58	-34.95±0.58	-34.94±0.58
35	-5.34±0.04	-4.81	-5.23	-5.40				-36.02±0.31	-36.04±0.31	-36.03±0.31

995 \* considering the MgHCO<sub>3</sub><sup>+</sup> and/or MgCO<sub>3</sub><sup>o</sup> aqueous complexes (reported by Robie and

996 Hemingway (1973) based on the data of Langmuir (1965)).

997

998

999 Table 3. Standard state properties (25°C, 1 bar) of nesquehonite reported in the literature and  
1000 determined in this study, and standard state properties of dypingite determined in this study.  
1001 The standard state properties of aqueous species used to calculate the Gibbs free energy of  
1002 formation of nesquehonite and dypingite in the present study are reported in the lower table,  
1003 as are the equilibrium constants of the considered aqueous Mg complexes at 25°C.

<i>Nesquehonite [MgCO<sub>3</sub>·3H<sub>2</sub>O]</i>				
Source	$\Delta G_r^\circ$ (kJ/mol)	$\Delta G_f^\circ$ (kJ/mol)	$\Delta H_r^\circ$ (kJ/mol)	$\Delta H_f^\circ$ (kJ/mol)
this study	30.1±0.8	-1723.5±0.8	-17.17	-1981.5
Robie and Hemingway (1973)		-1723.8±0.5		-1977.3±0.5
Langmuir (1965)		-1726.6±2.1		
<i>Dypingite [Mg<sub>5</sub>(CO<sub>3</sub>)<sub>4</sub>(OH)<sub>2</sub>·8H<sub>2</sub>O]</i>				
this study	199.4±1.3	-6792.7±1.3		
<i>Aqueous Species</i>				
Source	Species	$\Delta G_f^\circ$ (kJ/mol)	S (J/mol/K)	$\Delta H_f^\circ$ (kJ/mol)
Wagman et al (1982)	H <sub>2</sub> O	-237.13	69.95	-285.83
Shock and Helgeson (1988), Shock et al (1997)	Mg <sup>2+</sup>	-453.98	-138.07	-465.96
Shock and Helgeson (1988)	CO <sub>3</sub> <sup>2-</sup>	-527.98	-50.00	-675.24
Wagman et al (1982)	HCO <sub>3</sub> <sup>-</sup>	-586.77	91.20	-691.99
Wagman et al (1982)	OH <sup>-</sup>	-157.24	-10.75	-229.99
<i>Aqueous Complexes</i>				
Source	Species	<i>log K</i>	Reaction	
Stefansson et al (2014)	MgHCO <sub>3</sub> <sup>+</sup>	1.1	Mg <sup>2+</sup> + HCO <sub>3</sub> <sup>-</sup> ⇌ MgHCO <sub>3</sub> <sup>+</sup>	
Stefansson et al (2014)	MgCO <sub>3</sub> <sup>°</sup>	3.0	Mg <sup>2+</sup> + CO <sub>3</sub> <sup>2-</sup> ⇌ MgCO <sub>3</sub> <sup>°</sup>	
Palmer and Wesolowski (1997)	Mg(OH) <sup>+</sup>	-11.7	Mg <sup>2+</sup> + H <sub>2</sub> O ⇌ MgOH <sup>+</sup> + H <sup>+</sup>	
PHREEQC V3 LLNL database	MgCl <sup>+</sup>	-0.1	Mg <sup>2+</sup> + Cl <sup>-</sup> ⇌ MgCl <sup>+</sup>	

1004

1005

1006 Table 4. Calculated saturation indices for nesquehonite and dypingite from an experimental  
 1007 study (Mavromatis et al., 2012) and a natural Mg-rich wetland (Power et al., 2014).

<b>Mg-carbonate precipitation experiments (data from Mavromatis et al. 2012)</b>				
<b>Experiment</b>	<b>Experiment type</b>	<b>Precipitated mineral</b>	<b>Saturation index</b>	
			<b>nesquehonite</b>	<b>dypingite</b>
Abio-A-1	Abiotic	Nesquehonite	-0.52	-2.10
Abio-A-5	Abiotic	Dypingite	0.06	2.19
Abio-A-10	Abiotic	Dypingite	-0.05	1.67
Abio-A-13	Abiotic	Dypingite	-0.16	1.09
Abio-B-18	Abiotic	Nesquehonite	-0.16	1.16
Abio-C-7	Abiotic	Nesquehonite	-0.16	1.31
Abio-C-9	Abiotic	Nesquehonite	-0.22	0.91
Abio-C-11	Abiotic	Nesquehonite	-0.16	1.28
Abio-C-12	Abiotic	Nesquehonite	-0.18	1.12
Abio-D1-8	Abiotic	Nesquehonite	-0.34	0.39
Abio-D1-18	Abiotic	Nesquehonite	-0.21	1.20
Abio-D2-8	Abiotic	Dypingite	-0.26	0.96
Abio-D2-23	Abiotic	Dypingite	-0.17	1.26
Abio-E-7	Abiotic	Nesquehonite	0.11	1.84
Abio-E-10	Abiotic	Nesquehonite	0.34	3.61
Abio-E-11	Abiotic	Nesquehonite	0.35	3.83
Abio-E-13	Abiotic	Nesquehonite	0.27	3.42
Bio-A-1	Biotic	Nesquehonite	-0.45	-1.62
Bio-A-5	Biotic	Dypingite	-0.03	1.05
Bio-A-8	Biotic	Dypingite	0.26	3.20
Bio-A-12	Biotic	Dypingite	0.30	3.78
Bio-A-15	Biotic	Dypingite	0.13	3.13
Bio-B-4	Biotic	Nesquehonite	0.08	3.11
Bio-B-6	Biotic	Nesquehonite	0.02	2.86
Bio-B-8	Biotic	Nesquehonite	-0.19	1.78
Bio-B-9	Biotic	Nesquehonite	-0.31	1.43
Bio-B-10	Biotic	Nesquehonite	-0.46	1.64
Bio-B-11	Biotic	Dypingite	-0.49	2.00

1008

1009

1010 Table 4 (continued). Calculated saturation indices for nesquehonite and dypingite from an  
 1011 experimental study (Mavromatis et al., 2012) and a natural Mg-rich wetland (Power et  
 1012 al., 2014).

<b>Mg-carbonate precipitation experiments (data from Mavromatis et al. 2012)</b>				
<b>Experiment</b>	<b>Experiment type</b>	<b>Precipitated mineral</b>	<b>Saturation index</b>	
			<b>nesquehonite</b>	<b>dypingite</b>
Bio-C-5	Biotic	Dypingite	-0.39	1.65
Bio-C-5	Biotic	Dypingite	-0.37	1.75
Bio-D-3	Biotic	Dypingite	-0.32	1.59
Bio-E-7	Biotic	Nesquehonite+Dypingite	-0.30	1.96
Bio-E-9	Biotic	Nesquehonite+Dypingite	-0.24	1.60
Bio-F-9	Biotic	Nesquehonite	-0.18	2.02
Bio-G-2	Biotic	Nesquehonite	-0.35	-1.01
Bio-G-6	Biotic	Nesquehonite	0.40	4.90
Bio-I-5	Biotic	Nesquehonite	-0.49	1.59
<b>Natural wetland (data from Power et al., 2014)</b>				
<b>Location</b>	<b>Precipitation circumstances</b>	<b>Precipitated mineral</b>	<b>Saturation index</b>	
			<b>nesquehonite</b>	<b>dypingite<sup>a</sup></b>
Atlin, North lobe of main wetland	microbial mats	Dypingite	-0.06	0.32
Atlin, South lobe of main wetland	microbial mats	Dypingite	-0.11	0.01

1013 <sup>a</sup>temperature of wetland water was 10°C, but dypingite  $K_{sp}$  used was for 25°C

1014



1015 **Figure Captions**

1016

1017 **Figure 1.** Fourier transform infrared spectroscopy (FTIR) data for selected samples. Spectra  
1018 are offset along y-axis. Intensities on the y-axis are in arbitrary units (a.u.).

1019

1020 **Figure 2.** X-ray diffraction patterns of initial nesquehonite used in the short-term (blue line)  
1021 and long-term (purple line) experiments. The location of peaks in the nesquehonite reference  
1022 pattern are indicated by black circles.

1023

1024 **Figure 3.** Scanning electron micrographs of solids. A) initial nesquehonite. B) Solid sample  
1025 after 1420 h at 5°C. C) Solid sample after 359 h at 25°C. D) Solid sample after 311 h at 35°C.

1026

1027 **Figure 4.** Fluid composition over time in all experiments. Fluid composition evolution for the  
1028 entire experimental duration: A) pH, B) Mg concentration, C) dissolved inorganic carbon  
1029 concentration (DIC). Fluid composition evolution for the first 600 h of each experiment: D)  
1030 pH, E) Mg concentration, F) DIC. Data from the 5°C, 25°C, and 35°C experiments are  
1031 indicated by gray triangles, black diamonds, and blue squares, respectively, and short- and  
1032 long-term experiments are indicated by filled and open points, respectively. Error is smaller  
1033 than symbols unless otherwise shown.

1034

1035 **Figure 5.** Logarithm of nesquehonite solubility products ( $K_{sp}^{nsq}$ ) versus reciprocal of  
1036 temperature (in Kelvin).

1037

1038 **Figure 6.** Relative stability of hydrated Mg-carbonates at 25°C. A)  $Mg^{2+}$  activity in  
1039 equilibrium with magnesite, hydromagnesite, dypingite, and nesquehonite as a function of

1040 pH. The total dissolved inorganic carbon concentration was fixed at 0.06 M, the Na  
1041 concentration was fixed at 0.16 M, and the Cl concentration was fixed at 0.10 M to reflect the  
1042 conditions in the experiments. B)  $Mg^{2+}$  activity in equilibrium with magnesite,  
1043 hydromagnesite, dypingite, and nesquehonite as a function of  $pCO_2$ . The pH was fixed at 9,  
1044 Na concentration was fixed at 0.16 M, and Cl concentration fixed at 0.10 M to reflect the  
1045 conditions in the experiments. Calculations were done using PHREEQC V3 and the modified  
1046 LLNL database, as described in section 2.4.

1047

1048 **ES-Figure 1.** X-ray diffraction patterns of reacted solids in the 5°C experiment over time.

1049 Major nesquehonite peaks are indicated by the letter “n.”

1050

1051 **ES-Figure 2.** X-ray diffraction patterns of reacted solids in the short-term 25°C experiment

1052 over time. Major nesquehonite peaks are indicated by the letter “n,” and dypingite peaks by  
1053 the letter “d.”

1054

1055 **ES-Figure 3.** X-ray diffraction patterns of reacted solids in the long-term 25°C experiment

1056 over time. Major nesquehonite peaks are indicated by the letter “n,” and dypingite peaks by  
1057 the letter “d.” The peak indicative of the dypingite stoichiometry of

1058  $[Mg_5(CO_3)_4(OH)_2 \cdot 8H_2O]$  is indicated by the label “d(8H<sub>2</sub>O).” The peaks of the unidentified

1059 dypingite-like phase are indicated by the label “d-l.” The appearance of more noise in some  
1060 patterns is attributed to lower maximum intensities for those data.

1061

1062 **ES-Figure 4.** X-ray diffraction patterns of reacted solids in the short-term 35°C experiment

1063 over time. Major nesquehonite peaks are indicated by the letter “n,” and dypingite peaks by  
1064 the letter “d.” The peak indicative of the dypingite stoichiometry of

1065  $[\text{Mg}_5(\text{CO}_3)_4(\text{OH})_2 \cdot 8\text{H}_2\text{O}]$  is indicated by the label “d(8H<sub>2</sub>O).”

1066

1067 **ES-Figure 5.** X-ray diffraction patterns of reacted solids in the long-term 35°C experiment

1068 over time. Major nesquehonite peaks are indicated by the letter “n,” and dypingite peaks by

1069 the letter “d.” The peak indicative of the dypingite stoichiometry of

1070  $[\text{Mg}_5(\text{CO}_3)_4(\text{OH})_2 \cdot 8\text{H}_2\text{O}]$  is indicated by the label “d(8H<sub>2</sub>O).” The appearance of more

1071 noise in some patterns is attributed to lower maximum intensities for those data.